

# JGR Solid Earth

## RESEARCH ARTICLE

10.1029/2022JB026294

### Key Points:

- Foreshock sequences follow an inverse Omori-law during which foreshock migration toward the final epicenter is observed
- The nucleation process scales inversely with normal stress and an experimental scaling is found for inverse Omori-law
- The seismic/aseismic energy release continuously increases during nucleation, highlighting that the nucleation process starts as fully aseismic to evolve toward a cascading process

### Correspondence to:

S. Marty,  
[sam92son@gmail.com](mailto:sam92son@gmail.com)

### Citation:

Marty, S., Schubnel, A., Bhat, H. S., Aubry, J., Fukuyama, E., Latour, S., et al. (2023). Nucleation of laboratory earthquakes: Quantitative analysis and scalings. *Journal of Geophysical Research: Solid Earth*, 128, e2022JB026294. <https://doi.org/10.1029/2022JB026294>

Received 9 JAN 2023

Accepted 15 MAR 2023

### Author Contributions:

**Conceptualization:** S. Marty

**Funding acquisition:** A. Schubnel

**Investigation:** S. Marty, A. Schubnel, H. S. Bhat

**Methodology:** S. Marty

**Software:** S. Marty








**Supervision:** A. Schubnel, H. S. Bhat

**Validation:** A. Schubnel, H. S. Bhat, J. Aubry, E. Fukuyama, S. Latour, S. Nielsen, R. Madariaga

**Writing – original draft:** S. Marty

**Writing – review & editing:** S. Marty, A. Schubnel

## Nucleation of Laboratory Earthquakes: Quantitative Analysis and Scalings

S. Marty<sup>1</sup> , A. Schubnel<sup>2</sup> , H. S. Bhat<sup>2</sup> , J. Aubry<sup>2</sup> , E. Fukuyama<sup>3,4</sup>, S. Latour<sup>5</sup> , S. Nielsen<sup>6</sup> , and R. Madariaga<sup>1</sup> 

<sup>1</sup>Rock and Sediments Mechanics Laboratory, Penn State University, State College, PA, USA, <sup>2</sup>Laboratoire de Géologie, Ecole Normale Supérieure, CNRS-UMR8538, PSL Research University, Paris, France, <sup>3</sup>National Research Institute for Earth Science and Disaster Resilience, Tsukuba, Japan, <sup>4</sup>Department of Civil and Earth Resources Engineering, Kyoto University, Kyoto, Japan, <sup>5</sup>Université Toulouse III – Paul Sabatier, Toulouse, France, <sup>6</sup>Department of Earth Sciences, Durham University, Durham, UK

**Abstract** In this study we use the precursory acoustic emission (AE) activity during the nucleation of stick-slip instability as a proxy to investigate foreshock occurrence prior to natural earthquakes. We report on three stick-slip experiments performed on cylindrical samples of Indian metagabbro under upper crustal stress conditions (30–60 MPa). AEs were continuously recorded by eight calibrated acoustic sensors during the experiments. Seismological parameters (moment magnitude, corner frequency and stress-drop) of the detected AEs ( $-8.8 \leq M_w \leq -7$ ) follow the scaling law between moment magnitude and corner frequency that characterizes natural earthquakes. AE activity always increases toward failure and is driven by along fault slip velocity. The stacked AE foreshock sequences follow an inverse Omori type law, with a characteristic Omori time  $c$  inversely proportional to normal stress. AEs moment magnitudes increase toward failure, as manifested by a decrease in  $b$ -value from  $\sim 1$  to  $\sim 0.5$  at the end of the nucleation process. During nucleation, foreshocks migrate toward the mainshock epicenter location, and stabilize at a distance from the latter compatible with the predicted Rate-and-State nucleation size. Importantly, the nucleation characteristic timescale also scales inversely with applied normal stress and the expected nucleation size. Finally, we infer that foreshocks are the byproducts of the nucleation phase which is an almost fully aseismic process. Nevertheless, the seismic/aseismic energy release ratio continuously increases during nucleation, highlighting that, the nucleation process starts as a fully aseismic process, and evolves toward a cascading process at the onset of dynamic rupture.

**Plain Language Summary** Shallow earthquakes are common phenomena that result from the rapid release of strain accumulated by rocks in the Earth's crust. Numerous studies have reported an increase in fault slip rate and seismic activity (i.e., foreshock activity) prior to the occurrence of earthquakes, providing a potential path to earthquake forecasting. However, many earthquakes lack of precursory signals and occur unexpectedly. Here, we report on microseismic activity prior to experimental earthquakes with the goal of better constraining the physical mechanisms that control the occurrence of foreshocks prior to earthquakes. The main message from this study is that experimentally reproduced earthquakes under relatively simple experimental conditions (single fault, no fluid) are systematically preceded by increasing foreshock activity. Foreshock sequences follow an inverse power law of time to failure, with larger foreshocks being triggered closer to the final epicenter as time to failure is approached. The characteristic time of the nucleation process scales inversely with applied normal stress. Finally, the relative energy released aseismically by fault slip prior to failure, although several orders of magnitude larger than the seismic energy released by microseismicity, decreases continuously during the nucleation process, which is a potentially valuable information for earthquake prediction, provided that foreshock sequences are detectable.

## 1. Introduction

The term “foreshocks” refers to small earthquakes that would occur nearby in time and space of a larger earthquake to come. Papazachos (1973) made the observation that when a sufficient number of foreshock sequences were synchronized to the time of their respective mainshock and then stacked, the seismicity rate increases as an inverse power law of time when approaching the nucleation. This law, called “the inverse Omori law,” had then provided a potential path to earthquake prediction. However, statistical models (Helmstetter & Sornette, 2003; Ogata, 1988) are able to reproduce most of the features attributed to foreshock sequences which was used as an

argument to suggest that foreshocks merely reflect stochastic rather than physical processes. The outstanding question is thus whether or not earthquakes are preceded by a slow, emerging nucleation phase before propagating dynamically or start as small instabilities that may eventually grow bigger. These two opposite views are termed the “preslip” and the “cascade” models respectively (Beroza & Ellsworth, 1996; W. Ellsworth & Beroza, 1995). In the latter scenario, the use of foreshocks as a predictive tool for the occurrence of a larger earthquake would be compromised.

At the scale of the Earth's lithosphere, the occurrence of foreshock sequences preceding large earthquakes is not ubiquitous but, nevertheless, has been reported in some cases (Abercrombie & Mori, 1996; Bouchon et al., 2011; L. Jones & Molnar, 1976; Kato & Nakagawa, 2014). Foreshock activity preceding large subduction earthquakes has been found to correlate with the occurrence of slow slip transients in the region close to the hypocenter (Kato et al., 2012; Ruiz et al., 2014). When examining the occurrence of foreshock sequences with respect to the geodynamic context, it has been demonstrated that faults subject to high-slip rates produce more foreshock sequences (Bouchon et al., 2013; McGuire et al., 2005). Moreover, compared with the ordinary seismicity, foreshocks present singular characteristics such as migration and acceleration prior to the mainshock (Kato, Fukuda, Kumazawa, & Nakagawa, 2016; Marsan et al., 2014). Therefore, it has been argued that foreshocks are a by-product of the larger nucleation phase of the upcoming mainshock. Indeed, earthquakes are dynamic instabilities which result from the weakening of frictional properties of a seismogenic fault that has started to slip. The relation between on-fault friction and slip provides the theoretical frame to understand how earthquakes nucleate. Based on either slip weakening or rate-and-state friction laws, theoretical (Campillo & Ionescu, 1997; Ida, 1972; Uenishi & Rice, 2003) and numerical models (Ampuero & Rubin, 2008; Dieterich, 1992; Rubin & Ampuero, 2005) have demonstrated that before propagating dynamically, slip initially develops on a localized, slowly growing zone, which is defined as the nucleation zone.

The rate and state equations introduce a characteristic slip distance  $D$  (often referred as to the critical slip distance  $D_c$ ), which is defined as the characteristic slip required for the state variable  $\theta$  to reach its steady state value following a perturbation in slip velocity. Typical laboratory-derived values of  $D$  are of the order of 1–100  $\mu\text{m}$ . Models that use the rate and state formulation predict that earthquakes nucleate on short time and space scales, of the order of milliseconds and meters respectively (Fang et al., 2010; Kaneko & Lapusta, 2008; Lapusta & Rice, 2003). In the former case, detecting earthquakes nucleation from geodetic or seismological measurements would likely be unreachable. Whether  $D$  is scale independent, and hence laboratory-derived values of  $D$  are appropriate for larger-scale natural earthquakes, or scale dependent is a subject of debate. The scaling of  $D$  with earthquake size is supported by laboratory studies which showed that  $D$  depends on scales inherent to the size of earthquakes such as long wavelength roughness of fault zones (Ohnaka, 2003) or gouge thickness (Marone, 1998). The scaling of  $D$  with earthquake size is also supported by seismological observations. Seismic inversions that use linear slip weakening friction laws (Ide & Takeo, 1997; Olsen et al., 1997) inferred values of  $D$  (of the order of the meter) that are orders of magnitude larger than the values of  $D$  measured in laboratory. This discrepancy stems from the fact that, in the linear slip weakening friction formulation, the characteristic slip distance  $D$  has a different meaning;  $D$  is defined as the slip required for the friction to drop to its residual value and, hence, include the whole slip history. It is worth noting that measurements of  $D$  from seismic data are likely to be biased toward higher values due to filtering out high-frequency seismic data and to modeling assumptions and limitations (Cocco et al., 2009; Tinti et al., 2009). Nevertheless, larger values of  $D$  would imply nucleation processes to happen at larger length and time scales, most likely detectable by geodetic and seismological instruments.

In the last 40 years, a large number of rock fracture and/or friction experiments (Kwiatk, Goebel, & Dresen, 2014; Lockner, 1993; McLaskey & Lockner, 2014; Ojala et al., 2004; Passelègue et al., 2017; Schubnel et al., 2007; Thompson et al., 2009) have revealed an important increase in the rate of acoustic emission (AE) triggering prior to failure and/or slip propagation, which has emphasized the possibility of earthquake forecasting at the laboratory scale (Johnson et al., 2021). Dedicated stick-slip experiments have also supported the conceptual view of earthquake nucleation, whether it is for experiments conducted at low normal stress conditions on polymer materials (Guérin-Marthe et al., 2019; Gvirtzman & Fineberg, 2021; Latour et al., 2013; Nielsen et al., 2010; Selvadurai & Glaser, 2015), on crustal rocks under bi-axial (i.e., unconfined) conditions (Fukuyama et al., 2018; McLaskey & Kilgore, 2013; Ohnaka, 2003; Ohnaka & Kuwahara, 1990; Okubo & Dieterich, 1984) or triaxial (i.e., confined and hence higher normal stress) conditions (Acosta et al., 2019a; Aubry et al., 2020; Harbord et al., 2017; Passelègue et al., 2017). Experimental works have also investigated changes in the frequency-magnitude distribution (i.e.,

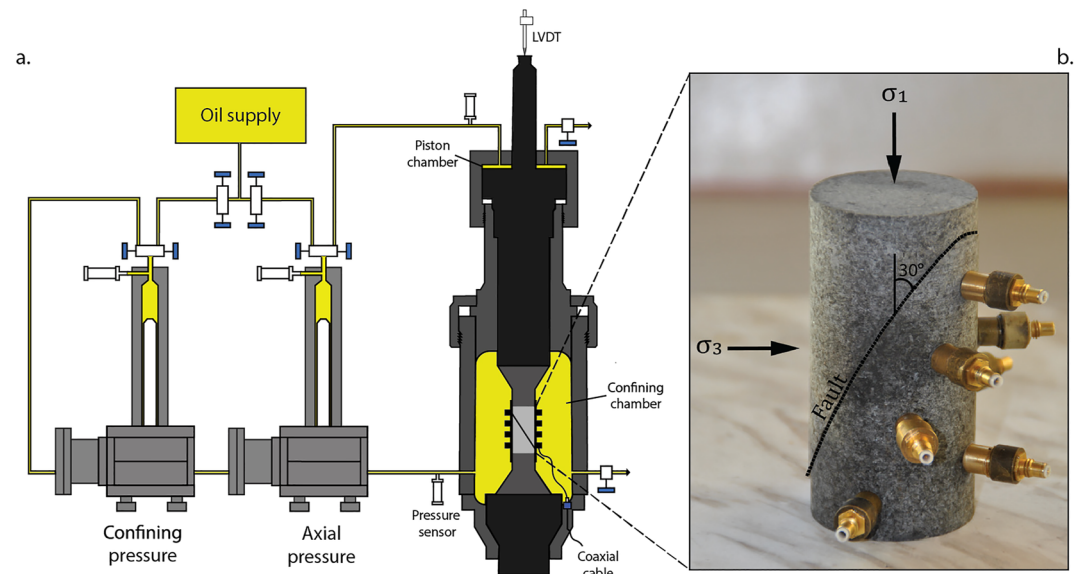


**Figure 1.** Triaxial apparatus and rock assemblage. (a) Schematic of the triaxial oil-medium loading cell. Two external servo pumps control axial and radial stresses. Axial displacement is given by the displacement of the piston measured by a LVDT at its top. (b) Saw-cut rock specimen used to reproduce laboratory earthquakes. The fault plane is oriented at  $30^\circ$  with respect to the principal stress  $\sigma_1$ . Seismic waves generated during the experiments are recorded by acoustic sensors glued at the surface of the sample.

the  $b$ -value or slope of the Gutenberg-Richter (GR) earthquake frequency-magnitude power law statistical relationship) of AEs during stick-slip cycles (Goebel et al., 2012; Lockner, 1993; Main et al., 1989; Sammonds et al., 1992). When the shear stress increases and the rupture is developing, a significant drop of the  $b$ -value has been reported, that is, the ratio between large and small AEs increases (Goebel et al., 2013; Lei et al., 2018; Rivière et al., 2018). This was thought to be driven by accelerating slip before dynamic rupture propagation. Consequently, this indicates that  $b$ -value changes could be used as a tool for seismic hazard assessment.

Despite all these efforts made to understand the driving forces of foreshock occurrence, the physical processes that govern their triggering are still controversial. It thus appears necessary to further constrain the length and time scales over which earthquakes nucleate, as well as the possible relation between foreshock and pre-slip during the nucleation phase. Here we report on precursory AE sequences during stick-slip experiments conducted on metagabbro saw-cut samples and under crustal stress conditions (30, 45, and 60 MPa). The purpose of this study is to use generated precursory AEs as a proxy to investigate the dominant mechanisms that control foreshock dynamics. We purposefully concentrate on stacked sequences of foreshocks, in order to highlight their general behavior, nevertheless keeping in mind the diversity and variability of the processes at play. Using calibrated acoustic sensors, AE seismological parameters (absolute moment magnitude, corner frequency, source size and stress drop) are estimated. AE features such as magnitude-frequency distribution, spatial distribution and temporal evolution toward failure are examined and interpreted. We find a scaling for the premonitory inverse Omori-law and finally, rely on absolute AE moment magnitudes to estimate the ratio between the seismic and the aseismic components of the pre-failure phase.

## 2. Experimental Procedure

Experiments were conducted on room dry cylindrical samples of Indian metagabbro, 88 mm long and 40 mm diameter. Samples contained a saw-cut surface inclined at an angle  $\theta = 30^\circ$  with respect to the vertical axis (Figure 1b). Saw-cut surfaces were ground flat and then manually roughen with a #240 sandpaper (average particle diameter 125  $\mu\text{m}$ ). The basic properties of metagabbro are as follows:  $P$ -wave,  $S$ -wave velocities, bulk density and shear modulus are respectively equal to  $c_p = 6.92 \text{ km/s}$ ,  $c_s = 3.62 \text{ km/s}$ ,  $\rho = 2980 \text{ kg/m}^3$ , and 35 GPa (Fukuyama et al., 2018).

Saw-cut samples were loaded in a triaxial oil-medium loading cell (Figure 1a). In each test: (a) the sample was placed in a 125 mm long and 4 mm thick viton jacket to isolate it from the confining fluid and positioned in the

confining chamber, (b) the confining pressure ( $P_c$ ) was applied and (c) the axial stress was increased by moving the vertical ram against the top of the sample at a constant speed (10  $\mu\text{m/s}$ ). Axial piston displacement and confining pressure were both independently servo-controlled. Axial stress and confining pressure were measured with external load cells with  $10^{-3}$  MPa resolution and axial shortening was measured at the top of the axial piston using a LVDT displacement sensor with  $\pm 0.1$   $\mu\text{m}$  resolution. Confining pressure, axial stress and axial shortening were recorded at 10 Hz during the experiments. More details on the mechanical set-up can be found in Schubnel et al. (2005).

Samples were instrumented with an array of 8 acoustic sensors positioned on one side of the fault plane (Figure 1b). Each acoustic sensor consisted of a cylindrical piezoelectric crystal (PZT—lead zirconate titanate) 5 mm in diameter and 0.5 mm thick (PI ceramic PI255) encapsulated in a brass casing. The acoustic sensors were glued directly to the sample through pre-drilled holes in the jacket and detected motion normal to the surface of the sample.

During each test, unamplified signals from the 8 acoustic sensors were relayed to a 16 bit digital oscilloscope (richter streaming system, from Amplifier Solution Corp) and recorded at 10 MHz sampling rate in a triggered mode. Unamplified waveforms were stored in blocks of 409.6  $\mu\text{s}$  (with an overlap of 102.4  $\mu\text{s}$ ) as long as the output voltage of one sensor exceeded a predefined threshold (20 mV). In parallel, signals from the 8 sensors were amplified at 45 dB (from Amplifier Solution Corp) before being relayed to a second 16-bit digital oscilloscope and continuously recorded at 10 MHz sampling rate. The purpose of recording the sensor signals at two different gains was to capture the large amplitude AEs generated by the stick-slip as well as the microseismicity (i.e., small amplitude AEs) before and after stick-slip. AEs were searched within the continuous waveforms with a simple amplitude threshold algorithm: continuous waveforms were scanned with a 406.9  $\mu\text{s}$  (i.e., 4,096 samples at a sampling rate of 10 MHz) long moving time window and the acoustic waveforms were stored if any amplitude of the acoustic signal exceeded the predefined threshold on two or more channels. For each channel, the amplitude threshold was set to 1.5 times the noise level which was purposefully low in order to capture a maximum number of AEs and to build complete AE-waveforms catalogs. AE detection results were then double checked by hand in order to eliminate false detections. More details on the acoustic recording set-up and processing can be found in Brantut et al. (2011) and Passelègue et al. (2017).

### 3. Methodology

#### 3.1. Fault Stress and Fault Slip Calculation

Axial displacement  $D$  recorded at the top of the axial piston is equal to the sum of the fault displacement  $\delta$  projected along the vertical axis and the elastic response  $X$  of the sample and piston column such that:

$$D = \delta \cdot \cos(\theta) + X \quad (1)$$

with  $\theta$  the angle between the normal of the fault plane and the axial stress  $\sigma_1$ .  $X$  corresponds to the elastic response of the combined system (sample + piston column) and is given by the ratio between the applied load  $L$  and the apparent stiffness  $k_a$  of the system:

$$X = \frac{L}{k_a} \quad (2)$$

Therefore, fault slip  $\delta$  can simply be calculated as follows:

$$\delta = \frac{D - L/k_a}{\cos(\theta)} \quad (3)$$

In practice, we made the assumption that the fault was fully locked (i.e.,  $\delta = 0$ ) at the beginning of each stick-slip cycle.  $k_a$  was determined from the slope of the linear elastic relationship between axial stress and axial displacement ( $k_a = L/D$ ), at 25% of peak stress during the inter stick-slip event (SSE) period. Since  $k_a$  is susceptible to change with cumulative displacement, its value was updated at the beginning of each stick-slip cycle. Shear stress ( $\tau$ ) and normal stress ( $\sigma_n$ ) acting on the fault were then derived from Mohr circle equations:

$$\tau = \frac{(\sigma_1 - P_c)}{2} \sin(2\theta) \quad (4)$$



$$\sigma_n = \frac{(\sigma_1 + Pc)}{2} + \frac{(\sigma_1 - Pc)}{2} \cos(2\theta) \quad (5)$$

with  $\sigma_1$  the axial stress and  $Pc$  the confining pressure. Finally, friction is simply given by  $\mu = \tau/\sigma_n$ .

### 3.2. AE and Stick-Slip Event (SSE) Hypocenter Location

For each stick-slip cycle, premonitory AEs and SSE-hypocenter were located by using a standard grid search method. The grid search analysis was restricted to a 2-D plane matching the elliptical saw-cut fault. The 2-D source location on the fault plane is given by the minimum of the L2 norm of the misfit,  $M_i(x, y)$ , between observed and theoretical  $P$ -wave arrival time differences ( $\Delta t_{i,j}^{obs}$ ,  $\Delta t_{i,j}^t$  respectively) for each pair of sensors ( $i, j$ ). For each grid node,  $M_i$  takes the form:

$$M_i(x, y) = \frac{\sum_{j=1}^n \sqrt{\sum_{j=1}^{n-1} (\Delta t_{i,j}^{obs} - \Delta t_{i,j}^t)^2}}{n(n-1)} \quad (6)$$

with  $n$  the number of sensors, ( $i, j$ ) the pair of stations and ( $x, y$ ) the cartesian coordinates of the grid node. Theoretical arrival times were calculated using an isotropic  $P$ -wave velocity  $c_p$  model.  $P$ -wave arrival times were first picked automatically using an Akaike Information Criterion (AIC) picking algorithm and then manually checked. Only AEs and SSE-hypocenters with location uncertainty lower than  $\sim 2$  mm ( $0.3 \mu s$  time residual) were retained in our location maps.

### 3.3. Acoustic Sensor Calibration

AE waveforms  $S(t)$  may result from the convolution of three different terms:

$$S(t) = f(t) * G(t) * R(t) \quad (7)$$

where  $f(t)$  is the source term,  $G(t)$  is the impulsive response of the medium (or so-called Green's function) and  $R(t)$  is the sensor response (i.e., the instrumental response). The purpose of calibrating an acoustic sensor is to characterize  $R(t)$  which defines the response of the sensor to a mechanical input quantity (stress, displacement, velocity of acceleration).

The AE sensors used in this study were calibrated prior to the experiments, using a high-frequency laser interferometer. Figure 2a displays a photograph and a schematic of the calibration set-up: an industrial (V109-rm or M110-sm, Olympus)  $P$ -wave transducer was positioned at the center of the saw-cut surface of the metagabbro sample and excited with a pick to pick 200 V sinusoidal wave. The generated wavefield was recorded on the opposite side of the sample, as particle velocity normal to the surface, with a laser interferometer (VibroOne, Polytec company) with a gain of 400 mm/s/V and a flat frequency response up to 2.5 MHz. One of the experimental (home-made) AE sensor was then glued to the sample at the location sampled by the laser. The transmitting transducer was similarly excited and surface vibrations were recorded again with the AE sensor. The instrumental response of the AE sensor  $R_s(\omega)$  (V/mm/s) was then obtained in the frequency domain, in the range DC to 2.5 MHz, by simple deconvolution of the waveform recorded by the AE sensor  $S_a(\omega)$  out of the waveform recorded by the laser  $S_v(\omega)$ :

$$R_s(\omega) = \frac{S_a(\omega)}{S_v(\omega)} \quad (8)$$

We explored calibration results reliability by varying (a) the type of transmitting transducer and (b) the frequency of the sinusoidal voltage applied to the transmitting transducer (500 kHz, 1 MHz, and 2 MHz). Transmitting transducers were of two types, namely V109-rm and M110-sm designed by Olympus company. These two transducers differ in size and shape but share similar characteristics: they produce longitudinal ( $P$ -)waves of 5 MHz central frequency. V109-rm has an L-shape and a nominal element size of 13 mm and M110-sm has a straight shape and a nominal element size of 6 mm. Calibration results are summarized in Figure 2b. For a specific transmitter, we found that the excitation frequency had a negligible effect on the sensor's response (Figure 2b, two top panels). Regardless of the type of transmitter, the receiver's (i.e., the sensor to be calibrated) response was non linear with a clear resonance band between  $\sim 1.2$  and 2.2 MHz. We found that, except for the width of the reso-

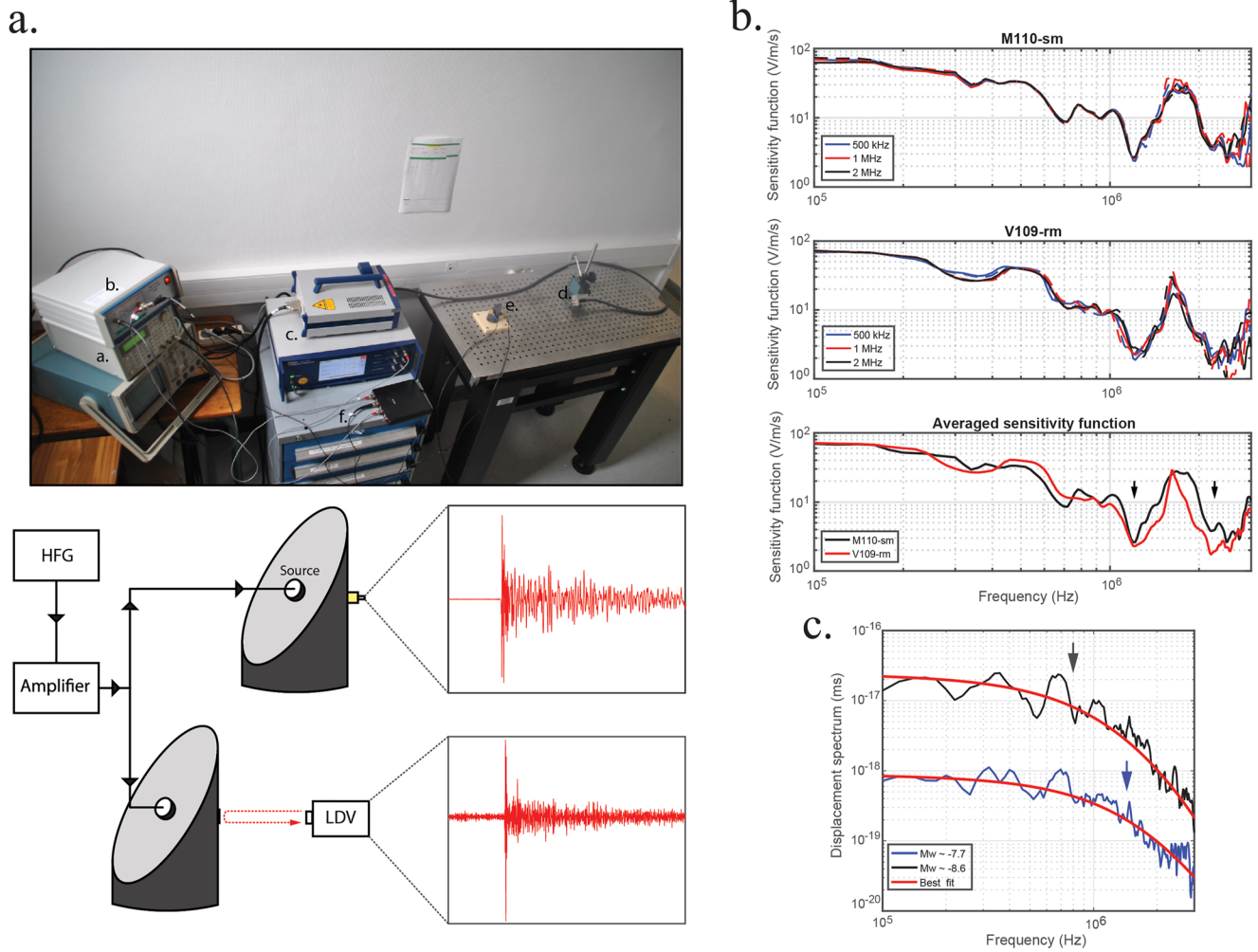


**Figure 2.** (a) Photograph and schematic of the experimental set-up used to calibrate the acoustic sensors. (b) Calibration results. The two top panels show, for the two transmitter types (M110-sm and V109-rm), the sensitivity functions obtained for the three tested excitation frequencies (500 kHz, 1 MHz and 2 MHz). Transmitters were excited with a 200 V pick-to-pick sinusoidal wave. The sensitivity functions averaged over the excitation frequencies are displayed in the bottom panel. (c) Fits of the displacement spectra of a  $M_w = 7.7$  acoustic emission (AE) and a  $M_w = 8.6$  AE. Estimated corner frequencies are indicated by the black arrows and are respectively 0.88 and 1.5 MHz.

nance band, the type of transmitter had little impact on the shape and amplitude of sensor sensitivity (Figure 2b bottom). Because we expected AE source size to be of the order of a few mm, we opted to use the instrumental response derived from the calibration set-up with the smallest source, that is, M110-sm. An important limitation of our calibration procedure is that it is probable that the instrumental response determined under atmospheric pressure might differ to the one under experimental pressure conditions. In particular, we expect the sensitivity of the sensor to increase, particularly at high frequency, under high pressure conditions, due to increasing sensor/rock coupling. At the same time, it is probable that sensor resonance is damped by the high pressure oil used as a confining medium. These effects have not been investigated.

For each AE recorded during the experiment, the velocity spectrum  $\Omega_v(\omega)$  was calculated by simple deconvolution of the AE waveform spectrum  $S_a(\omega)$  with the instrumental response  $R_a(\omega)$  such that:

$$\Omega_v(\omega) = \frac{S_a(\omega)}{R_a(\omega)} \quad (9)$$

Ultimately, the displacement spectrum,  $\Omega_d(\omega)$ , from which AE source parameters were derived (see next section), was obtained by integration in the frequency domain:

$$\Omega_d(\omega) = \frac{\Omega_v(\omega)}{2\pi\omega} \quad (10)$$

### 3.4. Inversion of AE Source Parameters

For each AE, absolute moment magnitude  $M_w$ , corner frequency  $f_c$ , static stress-drop  $\Delta\sigma$  and source radius  $r$  were derived from the stacked  $S$ -wave displacement spectrum. Single-sensor displacement spectra were obtained from a 27.5  $\mu$ s long time-window starting 2.5  $\mu$ s before the  $S$ -wave arrival. The first 2.5  $\mu$ s were multiplied to a ramp function to minimize the effect of  $P$ -wave energy on the results, the resulting signal was rescaled to a 50  $\mu$ s long time window centered on  $S$ -wave arrival and multiplied to a Hann window. Note that theoretical  $S$ -wave arrival was calculated according to the source-receiver distance and the  $S$ -wave velocity of the rock sample.

$S$ -wave spectra  $\Omega_s$  were modeled using a Brune source model with an attenuation term such as:

$$\Omega_s(f) = \frac{\Omega_0}{1 + (f/f_c)^2} \exp(-\pi f t/Q) \quad (11)$$

where  $\Omega_0$  is the long-period spectral plateau,  $t$  is the  $S$ -wave travel time averaged over all the sensors,  $Q$  the attenuation factor and  $f_c$  the corner frequency.  $f_c$ ,  $\Omega_0$ , and  $Q$  were estimated by grid search in the ranges of 100 kHz to 2.5 MHz,  $10^{-18}$  to  $10^{-15}$  m s $^{-1}$  and 30 to 50 respectively. The range of values for  $Q$  was selected according to values found in literature (Goldberg et al., 1992; Liu & Ahrens, 1997; Yoshimitsu et al., 2014) and was intentionally narrow to avoid significant trade-offs between  $Q$  and  $f_c$  that both control the high-frequency spectral decay.

The seismic moment  $M_0$  was computed from  $\Omega_0$  according to:

$$M_0 = \frac{4\pi}{\Lambda_{\theta,\phi}} \rho c_s^3 R \Omega_0 \quad (12)$$

where  $\rho$  is the bulk density,  $c_s$  the  $S$ -wave velocity,  $R$  the average distance between the source and the sensor and  $\Lambda_{\theta,\phi}$  the averaged  $S$ -wave radiation pattern (0.63, Aki and Richards 2002). From  $M_0$ , we get the absolute moment magnitude as:

$$M_w = (\log_{10}(M_0) - 9.1)/1.5 \quad (13)$$

We used the circular crack model of Madariaga (1976) to estimate the radius  $r$  from  $f_c$  such as:

$$r = \frac{0.21.C_S}{f_c} \quad (14)$$

Finally, the stress drop  $\Delta\sigma$  was calculated from  $M_0$  and  $r$  as (Eshelby, 1957):

$$\Delta\sigma = \frac{7M_0}{16r^3} \quad (15)$$

Figure 2c displays an example of fitted displacement spectra for two AEs of moment magnitudes  $M_w = 7.7$  and  $M_w = 8.6$ . The estimated corner frequencies are 0.88 and 1.5 MHz, source radii are 0.8 and 0.45 mm and static stress drops are 0.75 and 3.35 MPa respectively.

### 3.5. Estimation of $b$ -Value

AE frequency-magnitude distributions were modeled with a tapered GR distribution. The tapered GR relation has an additional exponential term with respect to the classical GR and is commonly expressed in terms of seismic moment  $M$ :

$$N(M) = N_t.(M_t/M)^\beta.\exp\left(\frac{M_t - M}{M_c}\right) \quad (16)$$

with  $N(M)$  the number of events with seismic moment larger than  $M$ ,  $N_c$  the number of events with seismic moment larger than the completeness seismic moment  $M_c$ ,  $M_c$  is the “corner” seismic moment that controls the distribution in the upper range of  $M$  and  $\beta$  is the exponent of the distribution which is equal to  $2/3$  of the  $b$ -value ( $\beta = \frac{2}{3}b$ ).  $\beta$  and  $M_c$  were estimated by grid search analysis (minimizing the misfit between model and observation) and  $b$ -value was obtained from  $\beta$ .

## 4. Experimental Results

### 4.1. Mechanical Data

Figure 3 displays friction, cumulative fault slip (stiffness corrected) and AE rate as a function of time during three experiments performed at  $P_c = 30, 45$ , and  $60$  MPa respectively. Experiments were stopped after  $8$  mm of cumulative displacement and a total of  $55$  SSEs,  $29$  SSEs, and  $13$  SSEs were produced at  $P_c = 30, 45$ , and  $60$  MPa respectively. The fault response to mechanical (constant far-field displacement) loading was similar at  $P_c = 30$  and  $45$  MPa (Figure 3, top 2 panels). The first SSE occurred when the static friction coefficient reached  $\sim 0.5$ . Then static (peak) friction coefficient and co-seismic stress-drop continuously increased up to the end of the experiments. Static (peak) friction increased from  $0.5$  to  $0.7$  and frictional stress-drop increased from  $\sim 0.05$  to  $\sim 0.1$  for both confining pressures. At  $P_c = 60$  MPa, the first SSE occurred when the static friction coefficient reached  $\sim 0.65$ . Unlike the other two experiments, static friction did not continuously increase with cumulative slip but rather fluctuated between  $\sim 0.65$  and  $0.72$ . Co-seismic frictional stress drop were also of the order of  $\sim 0.1$ . One interesting (and yet often disregarded) observation, is that while saw-cut faults were locked at the early stage of loading, they rapidly unlocked and began to slip, regardless of confining pressure. Indeed, stable fault slip started as early as the friction coefficient reached  $\sim 0.2$ – $0.25$  as illustrated by the change in the shear-stress and slip versus time slopes and a first SSE was generally required for the fault to enter a “pure” stick-slip behavior, that is, deform solely elastically during inter-event loading.

Three common features between the experiments are that AE activity remained concentrated in the last seconds prior to failure (as illustrated by the bursts of AE activity, Figure 3) and that the fault ruptured several times before generating AEs (low or no AE activity during the first couple of SSEs). It is interesting to point out that these experiments never produced aftershocks, even upon looking carefully within the continuous waveforms, which probably highlight the fact that the stress drop (and hence slip) had been rather homogeneous on the fault during the propagation of the mainshock. So all the detected AEs here can be considered as foreshocks. However, from a general point of view, we observed a great degree of variability in the AE foreshock activity, which tend to increase with increasing confining pressure conditions. For instance, while some SSEs produced no AEs at  $P_c = 60$  MPa, the highest rate of foreshock triggering ( $39$  AEs/s) was also recorded during this experiment. In contrast, foreshock activity at  $30$  MPa fell rapidly into a more predictable behavior characterized by a systematic AE rate increase prior to mainshock propagation.

### 4.2. AE Distribution

Figures 4a–4c display the number of AEs (dark color histograms), and the AE moment release (light color histograms) per stick-slip cycle at  $P_c = 30, 45$ , and  $60$  MPa respectively. In total,  $905, 380$ , and  $185$  AEs were recorded at  $P_c = 30, 45$ , and  $60$  MPa respectively, which equates to an average number of AEs per SSE of  $\sim 17, 13$ , and  $14$  respectively. The maximum number of AEs per SSE that were recorded is  $48, 31$ , and  $46$  at  $P_c = 30, 45$ , and  $60$  MPa respectively. We estimated that the maximum AE moment was of  $0.8$  N m at  $P_c = 30$  MPa and  $0.18$  N m at  $P_c = 45$  and  $60$  MPa. We observe here in more details that both the number of AEs and their cumulative moment remained quite variable during the experiments, although an increasing trend with cumulative slip can be observed, albeit less significant at  $P_c = 60$  MPa. The origin of this variability seemed uncorrelated either to the prior or the coming stress drop magnitude and will remain beyond the scope of the present study.

AE moment magnitude and AE seismic moment are displayed as a function of corner frequency in Figure 4d. Errorbars for corner frequency and moment magnitude are indicated in light gray. AE moment magnitudes range between  $\sim -8.6$  and  $\sim -7$ . For the large majority of the microseismicity, corner frequencies and stress-drops range from  $300$  kHz (source size  $\sim 4$  mm) to  $1.5$  MHz (source size  $\sim 0.5$  mm) and from  $0.1$  to  $10$  MPa with an average value for the stress-drop of  $1, 0.88$ , and  $0.68$  MPa at  $P_c = 30, 45$ , and  $60$  MPa respectively. A common observable is that larger AEs have larger stress-drops. The origin of this trend may result from the fact that, as will be seen

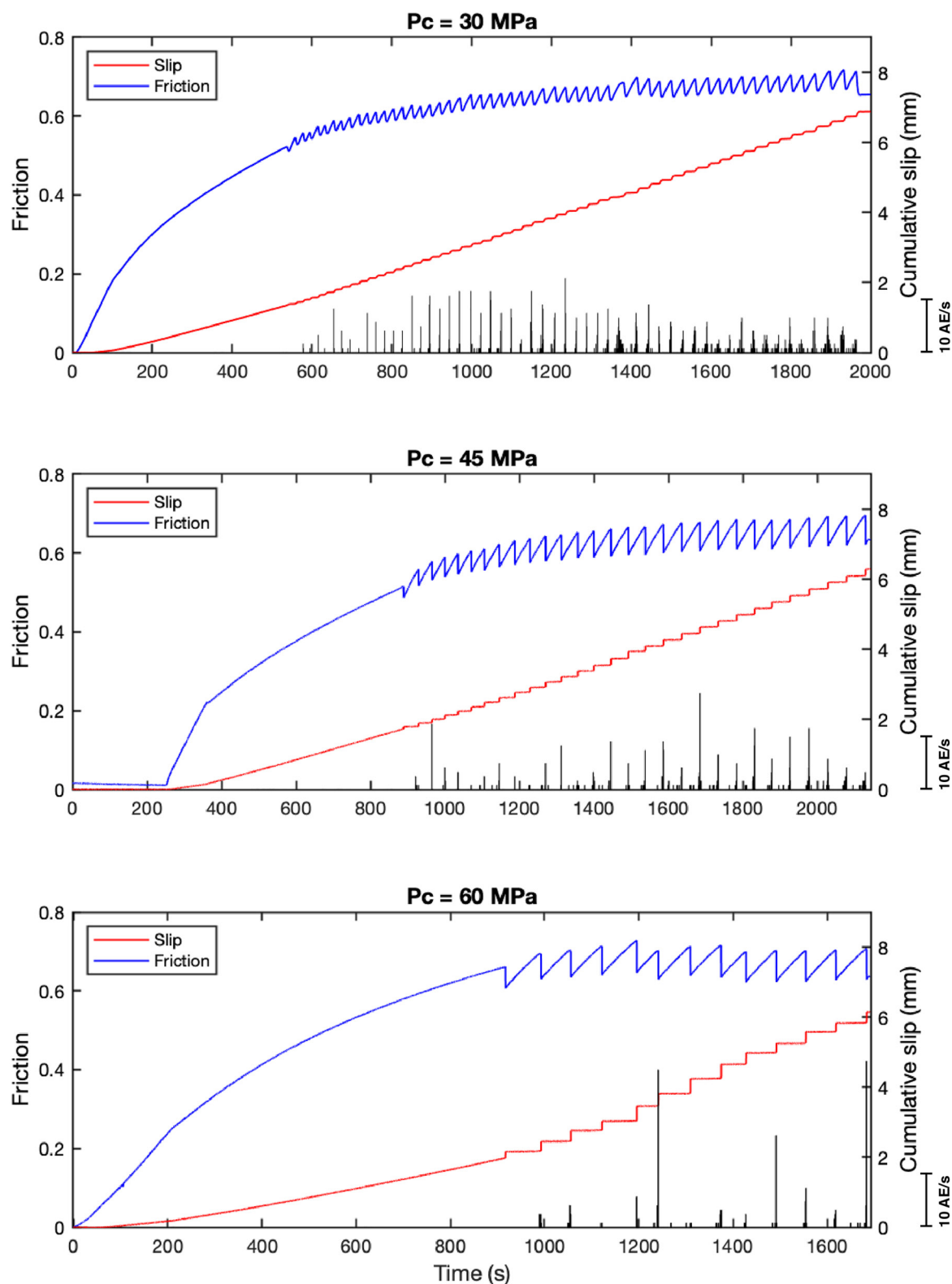


**Figure 3.** Cumulative slip, friction and acoustic emission rate during the experiments. Acoustic emissions were stacked into 1 s bins and cumulative slip was corrected from the elastic deformation of the column apparatus (sample + piston).



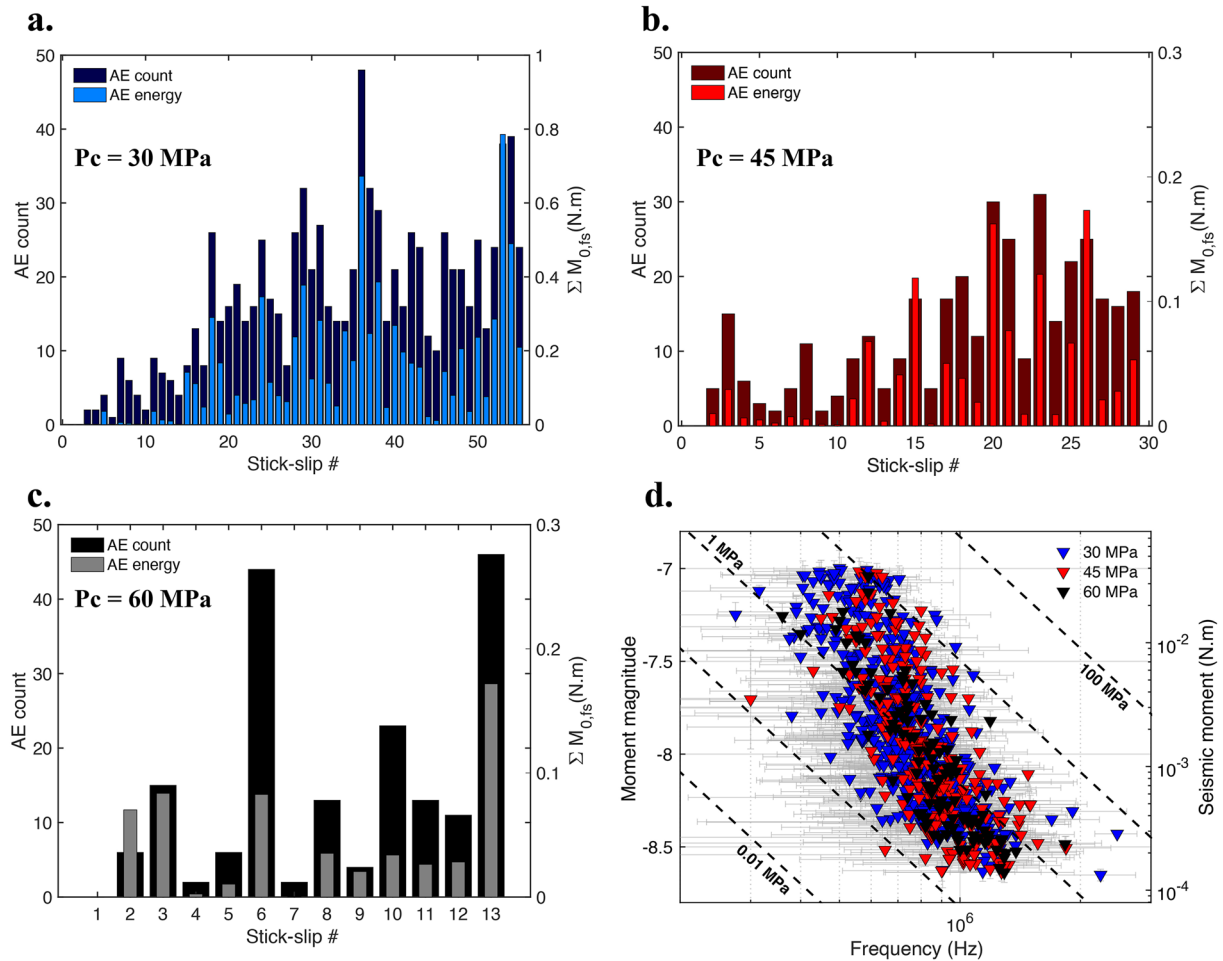


**Figure 4.** (a–c) Distribution of the number of acoustic emissions (AEs) (dark colors), and the total AE moment release (light colors) per stick-slip cycle for the three experiments. (d) Scaling relationship between AE seismic moments  $M_0$  (or equivalently moment magnitude  $M_w$ ) and AE corner frequencies  $f_c$ . Errorbars are shown in light gray. Dashed black lines represent stress drops of 0.01, 0.1, 1, 10, 100 MPa from Madariaga's source model (Madariaga, 1976).

in the next sections, larger AEs tend to occur closer to mainshock propagation, and, in such way, could in effect have larger stress drops as the fault surface approaches criticality and slip rate (and thus stress release) accelerates. Note that the possible bias mentioned above in our calibration procedure—the fact that high-frequency waves may propagate better under confinement than under room pressure, because both the attenuation of the rock medium will decrease as pre-existing cracks will close and so will the contact between the transducer and the rock surface—would tend to act in the opposite way. Indeed, one would have expected high-frequency amplitudes to be larger under confinement than under room pressure conditions, and in consequence, to overestimate the stress-drops of small magnitude (high-corner frequency) AEs. However, the evolution of transducer resonance may also have an effect, difficult to intuit, under confinement, another alternative being a frequency dependent quality factor.

### 4.3. Foreshock and Mainshock Hypocenter Locations

Photographs of the saw-cut faults after the experiments (left) with AE (circle symbols, middle) and SSE hypocenter (star symbols, right) locations are shown in Figure 5. Colorscale refers to SSE index and AE source sizes match source radii obtained by inversion. For a  $M_w = -7$  event and for a  $M_w = -8$  event, source size is typically of the order of 3 and 1 mm (similar to the average grain size of the sample:  $\sim 0.5$  mm) respectively. The largest amount of gouge was produced at the lowest stress condition ( $P_c = 30$  MPa). Wear product (white patterns, left photograph) aggregated into millimeter scale patches whose elongated shapes highlight the direction of sliding and whose typical length matches fairly well the fault cumulative displacement at the end of the experiment ( $\sim 8$  mm). Gouge clusters are

fairly homogeneously distributed on the fault plane, except near the fault edges where very little gouge was produced, which is a common feature to the three experiments. For the intermediate stress condition, gouge particles also gathered in elongated clusters in the sliding direction whose typical length corresponds well to fault cumulative displacement, however their spatial distribution is significantly more heterogeneous as illustrated by the dark spots where the fault remained almost intact (no wear production). It should be noted that post experiment, the two fault surfaces were always found symmetrical, so these spots without gouge are not due to possible gouge removal when the two pieces were separated after the tests. In contrast, gouge distribution is more homogeneous at the highest stress condition ( $P_c = 60$  MPa), during which wear material did not form clusters and sliding direction is hard to guess at that scale.

Although it is clear from the experiments conducted at  $P_c = 30$  MPa and  $P_c = 45$  MPa that AE locations correlate rather well with gouge distribution, gouge product does not necessarily implies AE activity. This last observable is well illustrated by the fault surface at  $P_c = 60$  MPa where a significant surface of the fault, while covered with gouge, did not produce AEs. SSE hypocenter locations migrated during the experiments, which is best illustrated at the two lowest stress conditions. SSE hypocenters initially located in the middle of the fault and then propagated to both ends of the fault at  $P_c = 30$  MPa. SSE hypocenters first located on the lower right edge of the fault and then migrated to the lower left edge at  $P_c = 45$  MPa. Regardless of the stress conditions, AE and SSE hypocenter locations and migrations match fairly well with one another. However, a noticeable mismatch between AE and SSE hypocenter locations is observed at the end of the experiment conducted at  $P_c = 30$  MPa.

#### 4.4. Microstructural Analysis

Fault surfaces were observed under scanning electron microscopy (SEM) after the experiments (Figure 6). From the images at the finest scale (Figures 6a, 6c, and 6e), we evaluate the range of gouge particle sizes to be between less than 1  $\mu\text{m}$  and few  $\mu\text{m}$ . Gouge particles cover asperity-like topographic heights, with size of the order of few tens of  $\mu\text{m}$  (Figures 6b, 6d, and 6f). While it is difficult to infer slip direction from geometric patterns at  $P_c = 30$  MPa, fault surfaces at  $P_c = 45$  and 60 MPa show evidence of thermally induced plastic deformation and melting processes, respectively, both of which captured the slip direction (Figure 6c–6f). At  $P_c = 45$  MPa, fault surface presents compacted and flatten microstructures (Figure 6c), aligned with the slip direction, which evidences that, locally at least, the fault surface temperature has nearly reached the melting point ( $\approx 1,200^\circ$ ). Finally, the elongated and stretched stringy microstructures observed at  $P_c = 60$  MPa (Figure 6e) is a robust proof of asperity melting of the fault surface during slip. The micro-crack (Figure 6d) perpendicular to slip direction that crosses the residual melt is likely due either to rapid cooling following melting or to co-seismic damage.

### 5. Discussion

#### 5.1. Nucleation Phase Dynamics

Figures 7a–7c compare the along fault displacement (blue curves), the along fault velocity (red curves), the cumulative number of AEs (black curves) and the cumulative AE moment release (dashed curves) with respect to time to failure at  $P_c = 30$ , 45, and 60 MPa respectively. The gray shaded area indicates the range of uncertainty for the cumulative AE moment release. Each quantity has been normalized by its maximum value at the time of failure and all the premonitory sequences have been stacked to highlight the general trend. Consistently with previous experimental studies (McLaskey & Lockner, 2014; Passelègue et al., 2017; Yamashita et al., 2021), we observed fault displacement preceding failure. However, although fault slip is required to generate foreshocks, both the number of foreshocks and their cumulative moment appear to correlate with slip velocity rather than slip itself. This is particularly well illustrated in the last seconds prior to failure during which cumulative moment release and fault slip velocity almost collapse regardless of the confining pressure.

The cumulative precursory foreshock activity per SSE is plotted versus time to failure at  $P_c = 30$ , 45, and 60 MPa Figures 7d–7f respectively. The black curve corresponds to the average sequence, while colored curves represent individual foreshock sequences, with the colorscale referring to the SSE index. Note that for visual inspection, not all AE sequences are shown at  $P_c = 30$  MPa (Figure 7d) and at  $P_c = 45$  MPa (Figure 7e). The experiment conducted at  $P_c = 30$  MPa gives the clearest example of what one would call “fault maturation” (Figure 7d). At the early stage of the experiment, most of the foreshocks occurred within seconds to failure, but with successive ruptures, precursory AE activity increased in number and occurred earlier during loading. Both at  $P_c = 30$  MPa and  $P_c = 45$  MPa, the number of foreshocks prior to failure only started to significantly increase after 10 stick-slip cycles.

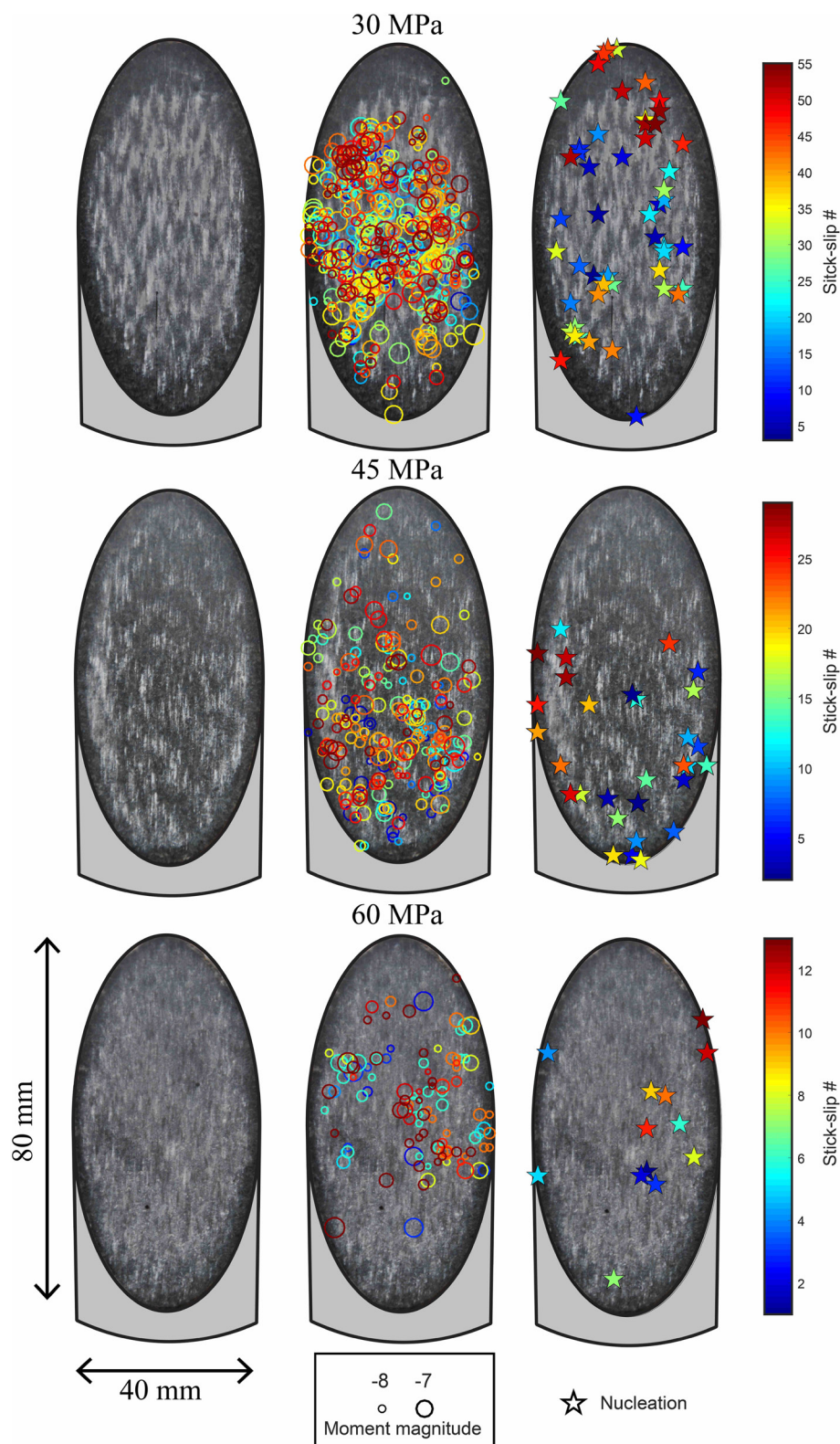


**Figure 5.** Post-experiment fault surfaces conditions (left), acoustic emission (AE) (center) and stick-slip event (SSE) hypocenter (right) locations. The size of the circles matches the estimated AE source sizes (assuming a circular shape) and the colorscale refers to the SSE index. Only AEs whose location errors are less than 2–3 mm are reported here.



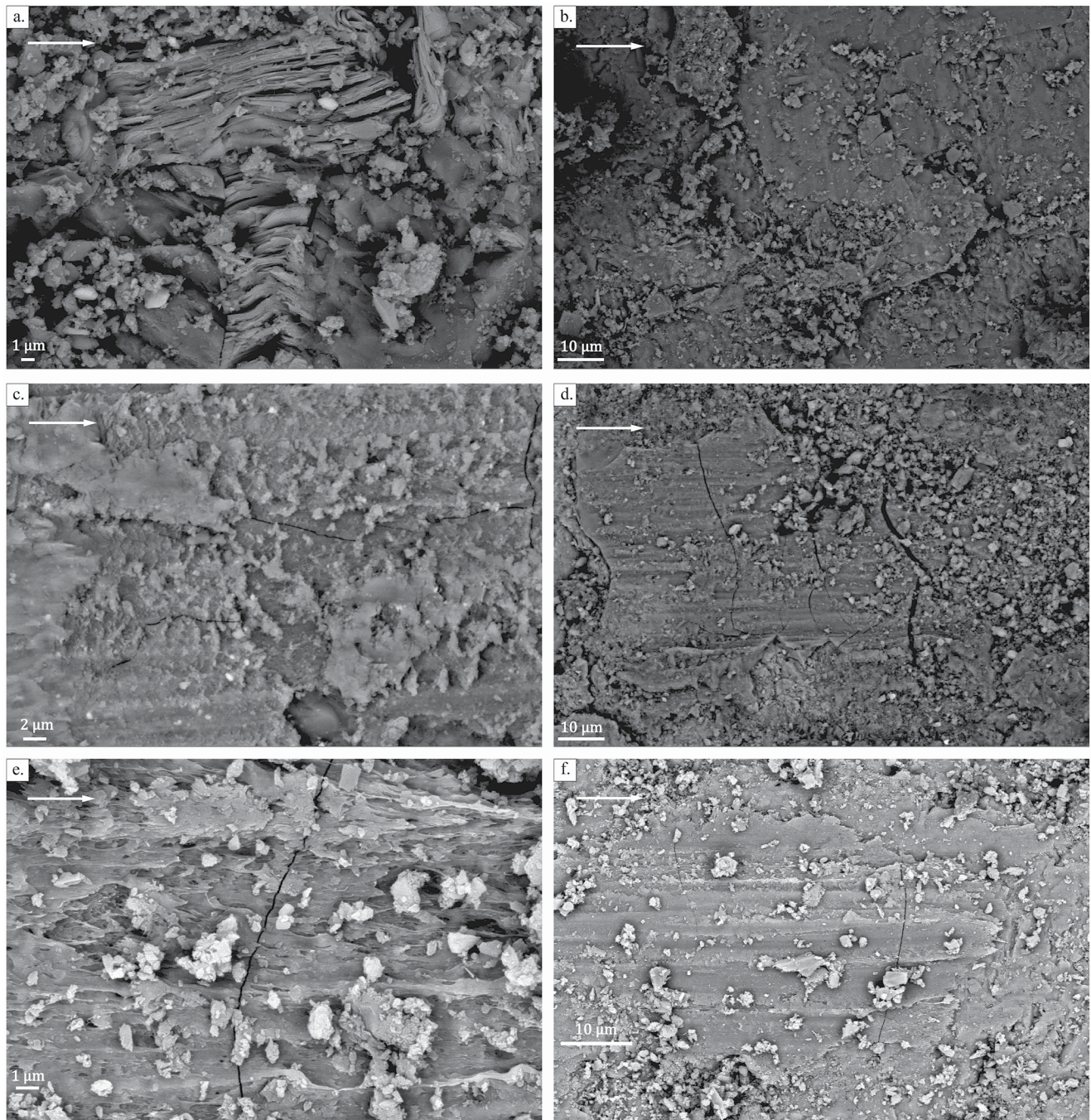


**Figure 6.** Post-experiment microtexture of the fault surfaces under Scanning Electron Microscopy at: (a, b)  $P_c = 30$  MPa, (c, d)  $P_c = 45$  MPa and (e, f)  $P_c = 60$  MPa. White arrows show the direction of sliding. (a) Small scale view of gouge particles with various sizes ranging from few  $\mu\text{m}$  to 100 nm. (b) Large scale view of (a) showing gouge patches heterogeneously distributed on a damaged asperity slightly deformed into the direction of sliding. (c) Small scale view of amorphous fine gouge particles layer. (d) Large scale view of (c) showing clusters of smashed gouge particles with sizes up to 10  $\mu\text{m}$ . The fault surface presents striations along the sliding direction which suggests plastic deformation during stick-slip events. (e) Small scale view of the fault surface showing evidence of partial melting during sliding. A fraction of the gouge particles is trapped into the melt. (f) Large scale view of (e) showing stretched and elongated surfaces formed due to partial melting and covered with (more) homogeneously distributed gouge particles.

Summing all AE sequences results in a smooth increase of the cumulative number of foreshocks as previously described. A noticeable difference lies in the absence of foreshocks early during loading at  $P_c = 60$  MPa. During this experiment, foreshocks occurred later, which results in a sharper acceleration of the cumulative number of foreshocks toward failure. On the other hand, the experiment conducted at  $P_c = 60$  MPa is the only one for which



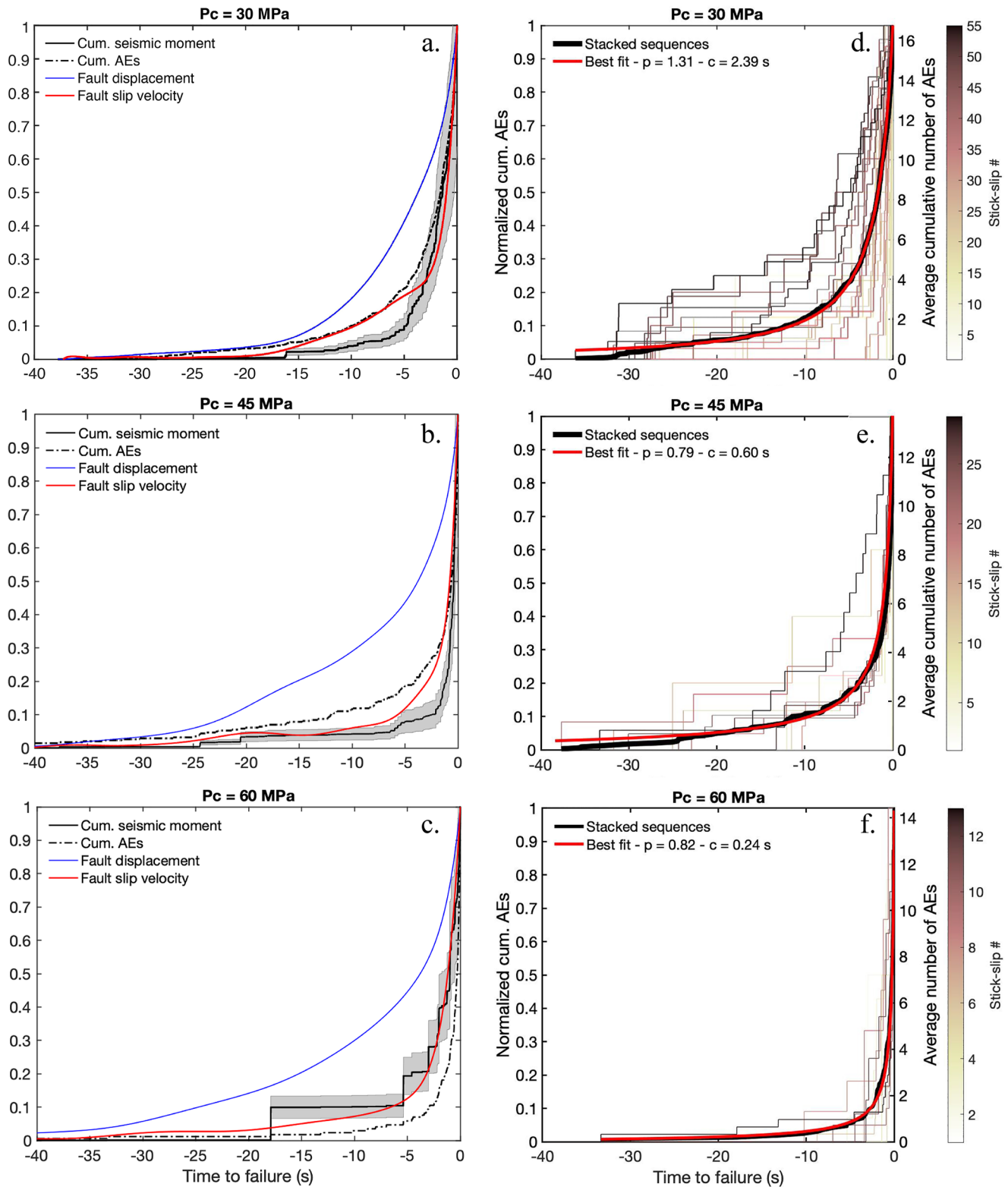


**Figure 7.** (a–c) Normalized fault displacement, fault velocity, cumulative number of acoustic emissions (AEs) and cumulative AE moment release in the last 40 s prior to failure at respectively  $P_c = 30$ , 45, and 60 MPa. Each curve represents stacking of all stick-slip event (SSE) sequences. (d–f) Inverse Omori fits (red curves) of the stacked cumulative number of AEs (black curves) in the last 40 s prior to failure at respectively  $P_c = 30$ , 45, and 60 MPa. The color curves display the individual precursory AE sequences, with the colorscale referring to the SSE index.



the first foreshocks have released a large amount of seismic energy early in the sequence, with respect to the ones that followed (Figure 7c).

## 5.2. Inverse Omori-Law

When averaged over numerous foreshock sequences, it is known that the foreshock rate  $N(t)$  increases as an inverse power law of the time to the mainshock (L. M. Jones & Molnar, 1979; Shearer et al., 2022) which, by analogy with the direct Omori's law, can be expressed as:

$$N(t) = \frac{K}{(c + \Delta t)^p} \quad (17)$$

where  $K$  is the foreshock productivity,  $c$  and  $p$  are empirical constants and  $\Delta t$  is the time to mainshock (or failure). Figures 7d–7f show the stacked cumulative number of foreshocks  $N_a(t)$  in the last 40 s prior to failure at  $P_c = 30$ , 45, and 60 MPa respectively. This allows us to highlight the smooth shape of the cumulative total number of AEs and to compare between the experiments the average number of precursory AEs during individual sequence.

The parameters  $p$  and  $c$  were searched in the range [0.1–3] with a step of 0.01. We made the choice to link  $K$  to  $c$  and  $p$  such as  $K = N_f \cdot (c^p)$  where  $N_f$  is the average cumulative number of AEs at the time of failure. This ensures that the average cumulative number of AEs at the time of failure equals  $N_f$ . The best fits were obtained for  $c = 2.39 \pm 0.3$  s and  $p = 1.31 \pm 0.08$ ,  $c = 0.6 \pm 0.25$  s and  $p = 0.79 \pm 0.1$  and  $c = 0.24 \pm 0.09$  s, and  $p = 0.82 \pm 0.05$  at  $P_c = 30$ , 45, and 60 MPa respectively.

In summary, we find that both  $p$  and  $c$  decreases with increasing normal stress (confining pressure). According to Equation 17 and using the best set of parameters obtained for  $c$  and  $p$ , we find that the average AE rate is about 5 times larger at  $P_c = 60$  MPa compared with  $P_c = 30$  MPa and about two times larger at  $P_c = 45$  MPa compared with  $P_c = 30$  MPa at the time of failure. This correlates well with the fault slip velocity. If we compare with the average fault slip velocity in the last 10 milliseconds we find that the fault slip velocity is about four times larger at  $P_c = 60$  MPa (about 4  $\mu\text{m/s}$ ) compared with  $P_c = 30$  MPa and about three times larger at  $P_c = 45$  MPa compared with  $P_c = 30$  MPa. Given the good correlation that we found between fault slip velocity and AE cumulative number (Figures 7a–7c), we posit that AE rate is primarily controlled by fault slip rate. However, it should be noted that this is only valid on average since precursory AE sequences exhibit variable behaviors with respect to each other.

We note two important factors that may bias our estimations of  $p$  and  $c$ , (a) we expressed  $K$  as a function of  $c$  and  $p$  and (b) we may have missed a significant number of AEs close to failure, either because of AEs occurring at the same moment and at the same location or because of small AEs that would be hidden by bigger ones. The most common way to estimate  $K$ ,  $c$ , and  $p$  is to use the maximum likelihood method (Ogata, 1983) which also quantifies the interdependence of  $K$ ,  $c$ , and  $p$ . Since we have expressed  $K$  as a function of  $c$  and  $p$  in the same way for each experiment and that  $N_f$  do not differ much ( $N_f$  equals 17, 13, and 14 at  $P_c = 30$ , 45, and 60 MPa respectively) we believe that linking  $K$  to  $c$  and  $p$  does not preclude interpreting the results relative to each other. Finally, AE catalogs magnitude completeness  $M_c$  in the last seconds prior to failure does not vary significantly with stress conditions ( $M_c \approx -8.4$ ). Therefore, missed AEs are likely to influence the absolute estimates of  $p$  and  $c$  but not their relative values.

## 5.3. Scaling With Nucleation Size

When derived from ETAS (Episodic Type AfterShock Sequence) models (Helmstetter & Sornette, 2003), the value of  $p$  is universal and close to unity. In ETAS models, the inverse Omori's law for foreshocks stems from the combination of the direct Omori's law (i.e., any earthquake triggers its own aftershocks) and the triggering of earthquakes in “cascade” mode due to stress (static or dynamic) transfer.

Figure 8a displays best fits for inverse Omori-law (dashed curves) super-imposed to stacked sequences fixing  $p = 1$ . In this case, the best values of  $c$  are  $c = 1.41$ , 0.92, and 0.35 s at  $P_c = 30$ , 45, and 60 MPa respectively, that is, a clear linear decrease of  $c$  with increasing normal stress at the onset of failure (inset in Figure 8a). Such observation is reminiscent of several experimental studies that have already proposed an inverse dependence of characteristic “nucleation” time with stress (Gvirtsman & Fineberg, 2021; Latour et al., 2013), while the inverse

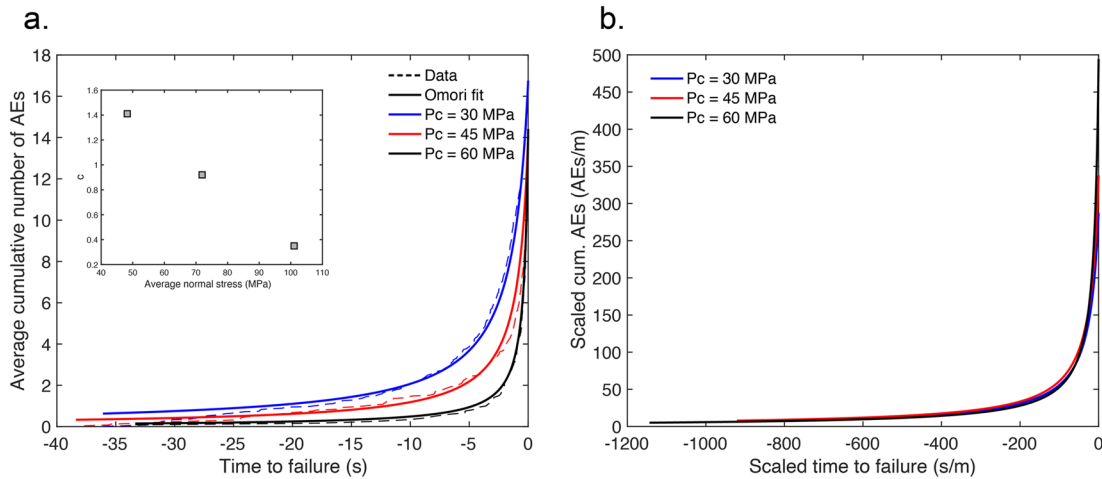


**Figure 8.** Scaling of the inverse Omori law. (a) Best inverse Omori fits (solid lines) of the stacked cumulative number of acoustic emissions (dashed lines) obtained by imposing  $p = 1$  at respectively  $P_c = 30, 45$ , and  $60$  MPa. The inset shows the linear relationship between  $c$  and normal stress with  $c = 1.41, 0.92$ , and  $0.35$  s at respectively  $P_c = 30, 45$ , and  $60$  MPa. (b) Inverse Omori fits scaled with the nucleation length  $L_b$  at respectively  $P_c = 30, 45$ , and  $60$  MPa. The curves collapse by normalizing the productivity  $K$  (y-axis) and the time to failure (x-axis) by  $L_b$ .

dependence of the  $c$ -value on stress conditions has also been inferred from natural aftershock data (Narteau et al., 2002, 2009).

A possible interpretation consistent with the above observation is if the characteristic nucleation time scales with the critical nucleation length  $L_c$ . For a linear slip weakening friction law (Campillo & Ionescu, 1997; Ida, 1972; Uenishi & Rice, 2003),  $L_c$  is defined as:

$$L_c = \beta \frac{\mu D_c}{\sigma_n (f_s - f_d)} \quad (18)$$

where  $\mu$  is the shear modulus of the rock sample,  $D_c$  is the critical slip distance,  $\sigma_n$  is the normal stress acting onto the fault,  $f_s$  and  $f_d$  are the static and the dynamic friction coefficients respectively and  $\beta$  is a non-dimensional shape factor coefficient ( $\approx 1.158$ ). Consequently,  $L_c$  is expected to decrease with increasing normal stress, as supported by stick-slip experiments on plastic polymers (Latour et al., 2013). Note that since friction decreases linearly with slip (i.e.,  $\Delta D/\Delta f$  is constant) in the linear slip weakening formulation, the values of  $D_c$  and  $(f_s - f_d)$  in Equation 18 are interchangeable with the amount of slip and the friction drop during the nucleation phase.

If  $L_c$  was significantly larger than the size of the fault for all experiments, the rock sample, regardless of stress conditions, would behave like a rigid block. The rock sample would accelerate uniformly prior to slip instability which would be controlled by the ratio between the loading stiffness and the critical fault stiffness. On the other hand, the fact that AEs tend to be distributed over the entire fault surface (Figure 5) and that the total area covered by foreshocks seems to decrease with stress conditions (Figure 5) suggests that  $L_c$  must be probably comparable to the experimental fault size. Taking  $D_c$  equals to the average pre-slip ( $\approx 5 \mu\text{m}$ ),  $\sigma_n$  equals to the average normal stress at the time of failure ( $\approx 50, 70$ , and  $100$  MPa at  $P_c = 30, 45$ , and  $60$  MPa respectively) and  $\mu = 35$  GPa, we find reasonable estimates (i.e., comparable or smaller than the fault total length size) of  $L_c$  equal to  $L_c = 80, 58$ , and  $40$  mm, respectively, only if  $(f_s - f_d) \geq 0.05$ . Although  $D_c$  is likely to be underestimated since it equals to the total displacement along the fault from the beginning to the end of loading,  $(f_s - f_d) \geq 0.05$  is a rather unreasonable estimate of friction drop during the nucleation phase.

An alternative is to calculate either of the critical nucleation lengths ( $L_{a-b}, L_b$ ) of the Rate and State friction law, defined as (Rubin & Ampuero, 2005):

$$L_{a-b} = \frac{\mu D_c}{(b-a)\sigma_n}; L_b = \frac{\mu D_c}{b\sigma_n} \quad (19)$$

where  $a$ ,  $b$ , and  $D_c$  are constitutive parameters. For Indian metagabbro,  $a$ ,  $b$ , and  $D_c$  were precisely determined under slow loading conditions ( $\sim 10 \mu\text{m/s}$ ), but albeit relatively low normal stress to be  $a = 0.005$ ,  $b = 0.009$ , and

$D_c \sim 1 \mu\text{m}$  (Urata et al., 2018). Under our experimental conditions, this would correspond to nucleation lengths  $L_{a-b} = 175; 125; 87 \text{ mm}$  and  $L_b = 78; 55; 38 \text{ mm}$  at  $P_c = 30, 45$ , and  $60 \text{ MPa}$  respectively. In conclusion, we find  $L_b$  to be the most consistent nucleation length estimate with our experimental observations, which is expected in the case of strong rate weakening (Viesca, 2016).

Now, scaling both the foreshock productivity and the time to failure with the nucleation length  $L_b$ , we find that foreshock sequences collapse onto a single inverse Omori master curve (Figure 8b). One can try to intuit what the scaled productivity (number of foreshocks/m) and the scaled time to rupture (s/m) represent physically. The latter may be interpreted as the inverse of fault slip velocity. It is interesting to point that the acceleration happens for a slowness of the order of  $\sim 100 \text{ s/m}$ , that is, a corresponding slip velocity in the range of cm/s, which is the typical slip-velocity at which thermal weakening processes start to be activated at the laboratory scale (Di Toro et al., 2011; Goldsby & Tullis, 2011; Rice, 2006). This is also in line with previous experimental works on stick-slip dynamics (Latour et al., 2013; Passelègue et al., 2016). The scaled foreshock productivity may in turn reflect the fault motion inside the nucleation zone, that is, the number of foreshock produced per amount of slip or advancement of the detachment front, which might be controlled by fault mechanical properties such as roughness for instance and, of course, loading conditions.

In summary, when taken individually, foreshock sequences are characterized by high variability which, as suggested theoretically (Lebihain et al., 2021; Schär et al., 2021) and experimentally (Gounon et al., 2022), is the manifestation of complex rupture nucleations on an heterogeneous fault interface. Because stacking the foreshocks sequences smooths this variability, our interpretation of the scaling on the inverse Omori law with normal stress/nucleation size, is thus that stacked foreshock sequences do indeed reflect the homogenized nucleation of the mainshock itself as conceptualized by Ohnaka's model (Ohnaka, 1992). From a qualitative perspective, if foreshocks are driven by the nucleation phase of the upcoming mainshock, their temporal distribution should satisfy a universal temporal distribution, which corresponds to the dynamics of the nucleation phase itself.

#### 5.4. Gutenberg-Richter $b$ -Value Temporal Evolution

We now look at the temporal evolution of the  $b$ -value of the stacked precursory AEs prior to failure (Figures 9a–9c) at  $P_c = 30, 45$ , and  $60 \text{ MPa}$  respectively.  $b$ -values were estimated within a moving window (with a tapered GR model, see Section 3.5) containing 100 AEs at  $P_c = 30, 45 \text{ MPa}$ , and 50 AEs  $P_c = 60 \text{ MPa}$ . Shaded areas indicate the 90% confidence intervals.

At  $P_c = 30 \text{ MPa}$  we estimate the  $b$ -value to be about 0.9 in the  $\sim 10 \text{ s}$  prior to failure. The  $b$ -value then dropped rapidly to reach an almost constant level  $\sim 0.4$  at the time to failure of  $t \sim 2 \text{ s}$ , which corresponds roughly to the  $c$ -value (dashed line) of the inverse Omori-law. The same is observed at  $P_c = 45 \text{ MPa}$ , during which the  $b$ -value was close to 1 up to  $\sim 10 \text{ s}$  prior to failure and then abruptly dropped to reach an almost constant level  $\sim 0.5$  at a time to failure of  $t \sim 1 \text{ s}$ , which again corresponds roughly to the  $c$ -value (dashed line) of the inverse Omori-law. For both experiments, the  $b$ -value remained constant and equal  $\sim 0.4$ – $0.5$  until failure. Unlike the other two experiments the  $b$ -value for the experiment conducted at  $P_c = 60 \text{ MPa}$  is initially low, close to 0.6, increases up to 0.8 and then decreases again to reach a value close to 0.5 in the last tenths of a second before rupture. However, the temporal evolution of the  $b$ -value prior to failure is less reliable during this experiment for at least two reasons: (a) the number of foreshocks was considerably lower (185, compared to 905 and 380 at  $P_c = 30$  and  $45 \text{ MPa}$  respectively) and (b) close to 90% of these were recorded in the last 3 s prior to failure which lowers considerably the temporal resolution of  $b$ -value variations in the early stages of the stick-slip cycles. In comparison about 30% and 25% of the total number of AEs were generated before entering the last 3 s prior to failure at  $P_c = 30$  and  $45 \text{ MPa}$  respectively.

Aki (1981) proposed a model where the fractal dimension of the fault plane is equal to  $\sim b/2$ . In which case, a  $b$ -value of 1 corresponds to productivity on a plane, while in his model, a  $b$ -value of 0.5 would correspond to fault lines filling up a plane. Based on the above observations, we can thus interpret the drop in  $b$ -value from  $\sim 1$  far away in time from rupture, to  $\sim 0.5$  at the onset of slip acceleration as a transition from foreshocks being produced on the entire fault plane, to foreshocks being the result of an accelerating slip front due to the rapid weakening of the fault interface close to failure. Temporal variations in  $b$ -value prior to failure have also been documented during fracture experiments conducted on intact rock samples (Lockner et al., 1991; Scholz, 1968) and during rock friction experiments (Goebel et al., 2012; Kwiatek, Goebel, & Dresen, 2014; Rivière et al., 2018). Fracture

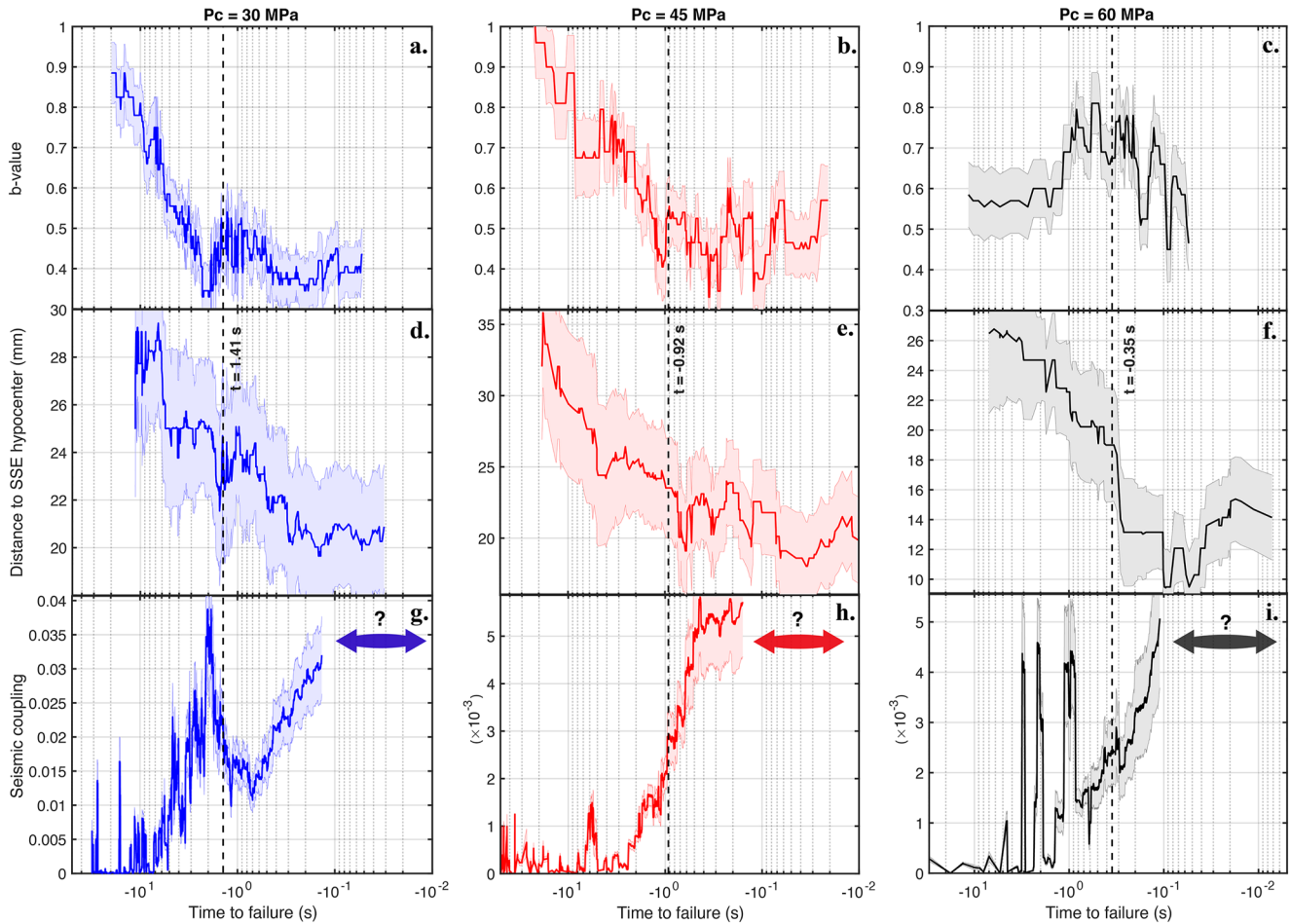


**Figure 9.**  $b$ -Value, precursory acoustic emission (AE) migration and seismic coupling as a function of the logarithm of time to failure. Dashed lines indicate the parameter  $c$  of the best Omori inverse models obtained by imposing  $p = 1$ . (a–c)  $b$ -value estimated within a moving window containing 100 AEs at  $P_c = 30$ , 45 MPa, and 50 AEs at  $P_c = 60$  MPa. Shaded areas correspond to the 90% confidence intervals. (d–f) Average distance to stick-slip event hypocenter of the precursory AEs computed within a moving window containing 50 AEs at  $P_c = 30$  and 45 MPa and 25 AEs at  $P_c = 60$  MPa. Shaded areas correspond to the  $\pm$  one standard deviation intervals. (g–i) Seismic coupling computed within a moving window of duration equal to 1% of the duration of the stacked precursory AE sequence. Shaded areas display the range of uncertainty computed from foreshock magnitude uncertainties. Double headed arrows indicate the time range for which seismic coupling cannot be estimated due to a temporal resolution of  $\sim 0.1$  s.

experiments on intact samples show that  $b$ -value and differential stress are anti-correlated, which takes its origin in the formation and the coalescence of microfractures. Such a process causes a large number of AEs to be generated and a smooth and accelerating drop of  $b$ -value up to the time of failure. Decrease in  $b$ -value toward failure has also been documented preceding large subduction earthquakes (Enescu & Ito, 2001; Nanjo et al., 2012; Suyehiro, 1966; Tormann et al., 2015). However, foreshocks that precede large earthquakes occur on time scales from hours to years. Long term variations of  $b$ -value are usually attributed to stress accumulation or partial stress release while short term variations are related to the mainshock nucleation.

### 5.5. Foreshock Migration

We now look at the evolution of the spatial distribution of foreshocks toward failure (Figures 9d–9f). Shaded areas indicate the  $\pm$  one standard deviation intervals. In what follows, “nucleation” refers to the mainshock hypocenter on the fault surface, which was determined using first  $P$ -wave arrival times (Figure 5, right panels). Mainshocks whose nucleation sites were poorly constrained (less than about 2–3 mm) were not taken into account in the following analysis. Note that, foreshocks located with more than  $0.3 \mu\text{s}$  travel time residuals (about 2–3 mm of location accuracy) were also disregarded.



Figures 9d–9f display the average distance to SSE hypocenter of the stacked precursory AEs as a function of time to failure at  $P_c = 30, 45$ , and  $60$  MPa respectively. Average distance to SSE hypocenter was computed within a moving window containing 50 AEs at  $P_c = 30, 45$  MPa, and 25 AEs at  $P_c = 60$  MPa. Note that decreasing the size of the window has no impact on the results other than to introduce high-frequency oscillations. At  $P_c = 30$  MPa, we see that the average distance of the foreshock sequence continuously decreases when approaching failure, to finally stabilize at an average of 25 mm to the eventual mainshock epicenters. The same is observed at  $P_c = 45$  and  $60$  MPa, during which the average distance of the foreshock sequence continuously decreases when approaching failure, to finally stabilize at an average distance of 20 and 15 mm respectively of the eventual mainshock epicenters. One should first note that, given the uncertainties, these values are compatible with our former estimates of  $L_p/2$ .

The spatial distribution of foreshocks yields relevant information about the way mainshocks initiate. In all experiments, we found that SSEs are always preceded by pre-slip acceleration phase. Moreover, we found that mainshocks do not necessarily nucleate where foreshocks concentrate, but rather at the edges of the areas where most of the precursory AE moment was released. Because of the drop in  $b$ -value discussed above, large precursory AEs, which tend to occur closer to failure, may promote a cascade-like process. Previous experimental studies (McLaskey, 2019; McLaskey & Lockner, 2014; Passelègue et al., 2017) proposed that pre-slip may sufficiently weaken fault strength to facilitate a small instability to grow large and eventually propagate over the entire fault. In such a scenario, precursory AE activity should migrate toward the mainshock epicenter in the last milliseconds prior to failure, as observed for the first time experimentally here.

### 5.6. Seismic Coupling During Nucleation

We now compute the evolution of fault coupling, that is, the ratio between the moment released by foreshocks (black curves in Figure 7) and that by fault slip (blue curves in Figure 7) as a function of time to failure. Fault coupling was computed within a moving window of duration equal to 1% of the duration of the stacked precursory AE sequence. The moment released by fault slip is simply computed as  $M_{0s} = G\pi ab\delta$ , where  $a, b$  are the long and short axis of the elliptical fault and  $\delta$  the fault slip. This ratio is plotted as a function of time to rupture for the three experiments at  $P_c = 30, 45$ , and  $60$  MPa (Figures 9g–9i respectively). Shaded areas display the range of uncertainty computed from foreshock magnitude uncertainties. In all three experiments, the cumulative moment release of foreshocks during nucleation represents only a very small percentage of the pre-seismic slip (Figures 9g–9i). Yet, it continuously increases during nucleation, from a fraction close to zero at the beginning of nucleation, to 3%, 0.5%, and 0.2% at the onset of failure at  $P_c = 30, 45$ , and  $60$  MPa respectively. Moreover, one can observe that the coupling increases drastically during the phase of nucleation when the distance of foreshocks to the epicenter as well as the  $b$ -value have stabilized. Before that, some transient increases in coupling are observed, mainly due to foreshocks occurring in bursts.

Our observations thus demonstrate that, at least in our experiments, the nucleation phase initiates as an almost fully aseismic process, and transitions, as time to failure approaches, toward a cascading process. In that interpretation, both the cascade and pre-slip models are not exclusive, as previously noted by McLaskey (2019). It is also interesting to note that the observed value of coupling at the onset of the mainshock decreases with increasing normal stress, which, again, is reminiscent of a shrinking of the nucleation size discussed above. In such case, the amount of fault area which radiates “seismically” at the final stage of nucleation can be interpreted as a lower bound for the nucleation size. The values of 3%, 0.5%, and 0.2% observed close to failure translate in a minimum nucleation length of  $\sim 10, \sim 4$ , and  $\sim 2.5$  mm, or, assuming a stress drop of 10 MPa, an equivalent moment magnitude of  $-5.4, -6.2$ , and  $-6.6$  at  $P_c = 30, 45$ , and  $60$  MPa respectively, which is larger than the largest foreshocks detected ( $M_w \sim -6.8$ ) in our experiments. Note that seismic coupling could not be resolved in the last tens of milliseconds (doubled headed arrows, Figures 9g–9i) due to insufficient temporal resolution ( $\sim 0.1$  s), thus the aforementioned minimum nucleation lengths are likely to be underestimated. One can attempt to extrapolate seismic coupling using the linear portions of the curves in the last second prior to failure. By doing so, we obtain values of  $\sim 6\%, 1.5\%$ , and  $1.2\%$  entering the last 10 milliseconds prior to failure (i.e.,  $10^{-2}$  s) at  $P_c = 30, 45$ , and  $60$  MPa, which equates to a minimum nucleation length of  $\sim 14, \sim 7$ , and  $\sim 6$  mm.

## 6. Scaling Laws and Implications for Natural Earthquakes

### 6.1. Pre-Seismic Moment and Seismic Coupling

Figure 10a compares the total foreshock moment release per mainshock  $M_{0a}$  with the pre-seismic moment release  $M_{0p}$ . Figure 10b shows pre-seismic moment release as a function of co-seismic moment release. Our data



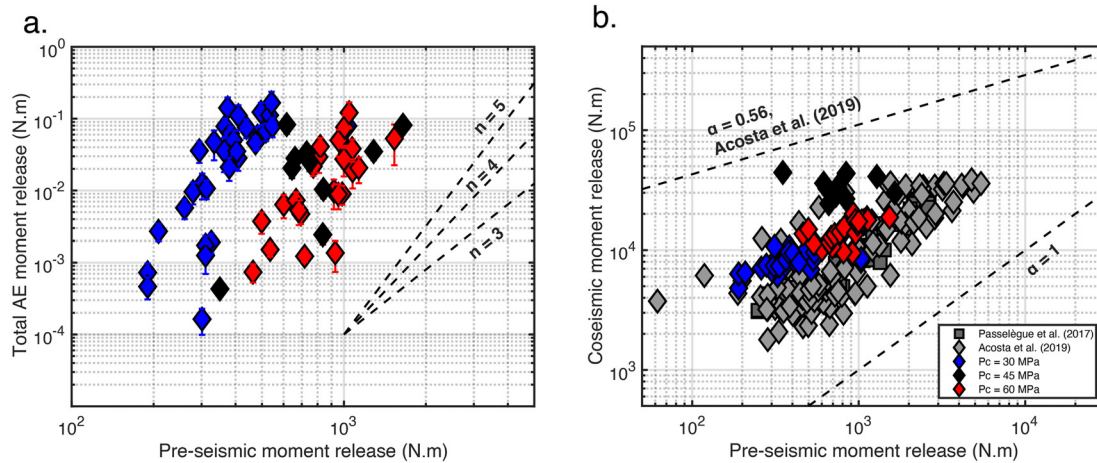


**Figure 10.** (a) Total acoustic emission moment release as a function of pre-seismic moment release. Each marker represents one stick-slip event. The black dashed lines show the slopes for power law type relations of exponent  $n = 4, 5$ , and  $6$ . (b) Co-seismic moment release as a function of pre-seismic moment release. As a comparison, the data from the present study (diamond symbols) are plotted together with the data (gray squares and circles) from two other experimental studies (Acosta et al., 2019b; Passelègue et al., 2017). The black dashed line with slope  $0.56$  corresponds to the scaling law between pre-seismic moment release  $M_p$  and co-seismic moment release  $M_c$  proposed by Acosta et al. (2019b). A linear relation between both quantity is given by the black dashed line with slope  $1$ .

(diamond symbols) are plotted together with the observations made by two previous experimental studies (Acosta et al., 2019b; Passelègue et al., 2017, gray symbols). Pre-seismic moment release and co-seismic moment release were estimated according to  $M_{0p,0c} = \mu D_{p,c} S$  with  $\mu$  being the metagabbro shear modulus,  $S$  the surface of the fault and  $D_p$  and  $D_s$  the pre-seismic slip and the co-seismic slip respectively.  $D_p$  is the total macroscopic fault slip accumulated between two successive mainshocks and thus includes pre-slip related with nucleation and potential fault creep. Here after, we refer as to “seismic coupling” the ratio between the total moment AE release  $M_{0a}$  and the pre-seismic moment release  $M_{0p}$ .

Seismic coupling ranges from about  $10^{-6}$  ( $10^{-4}\%$ ) to  $10^{-3}$  ( $0.1\%$ ). Regardless of stress conditions, we find a power law between  $M_{0a}$  and  $M_{0p}$  of the type  $M_{0a} \propto M_{0p}^n$ . Although, we acknowledge that data range and data quality preclude a robust estimate of the power law exponent  $n$ ,  $(3:5)$  seems a reasonable range of values (Figure 10a). In the case of an isotropic expansion of a self-similar crack of length  $L$ , the moment release inside the crack scales as  $\Delta\tau L^3$  or, equivalently, as  $\Delta\tau D_i^3$  (Madariaga, 1976) with  $D_i$  the amount of slip inside the crack. Thus the latter scenario predicts that  $M_{0a}$  goes as  $M_{0p}^3$  (i.e.,  $n = 3$ ) and is consistent with the interpretation made so far which is that mainshocks initiated as the emergence of an aseismically slipping fault patch that was driving precursory foreshock activity. The case  $n > 3$  can be explained if foreshocks have stress-drops that are magnitude dependent, that is higher stress-drops for larger magnitudes. Blanke et al. (2021) used the spectral ratio technique to precisely estimate AE stress drops and observed a significant increase in AE stress drop with AE size, which is a feature we also observe (Figure 4d).

Acosta et al. (2019b) argued that the pre-seismic moment release  $M_{0p}$  should scale with the co-seismic moment release  $M_{0c}$ . This scaling relationship is indeed expected if fracture energy increases as a power law of co-seismic displacement (Abercrombie & Rice, 2005; Ohnaka, 2013; Passelègue et al., 2016) such as:

$$G = \zeta u_{\text{cos}}^\alpha \quad (20)$$

where  $\zeta$  is a scaling pre-factor,  $\alpha$  is the scaling power-law exponent and  $u_{\text{cos}}$  is the co-seismic displacement. The following empirical scaling relation between  $M_{0p}$  and  $M_{0c}$  was proposed (indicated by the slope =  $0.56$ , Figure 10b):

$$M_{0p} \propto M_{0c}^{0.56} \quad (21)$$

In our experiments,  $M_{0p}$  contributes on average to about  $4\%$ ,  $6\%$ , and  $2\%$  of  $M_{0c}$  at  $P_c = 30, 45$  and  $60$  MPa respectively. This is slightly less than what was found by Passelègue et al. (2016) and Acosta et al. (2019b) but is typically of the same order of magnitude. Experimental observations may also simply indicate a linear relation between  $M_{0p}$  and  $M_{0c}$  as given by the slope of  $1$ .

## 6.2. Comparison With Natural Earthquakes and Implications

The scaling relationship between moment magnitude and corner frequency  $M_0 \propto f_c^{-3}$  is verified on the scale of crustal faults, induced seismicity or in the laboratory, that is, for a wide range of moment magnitudes from  $-8$  to  $8$  (Abercrombie, 1995; Aki, 1967; Blanke et al., 2021; Hiramatsu et al., 2002; Kwiitek et al., 2011; Prieto et al., 2004; Selvadurai, 2019; Yamada et al., 2007; Yoshimitsu et al., 2014). In line with previous studies, the estimated AE source parameters also satisfy this scaling relationship (Figure 4d). Therefore, foreshocks recorded during the experiments can truly be considered as micro-earthquakes which is determinant for extrapolating the inferences made in the laboratory to the scale of crustal faults. In a sense, foreshocks recorded during the experiments are more similar to natural earthquakes than mainshocks do, since they consist in self-terminating ruptures. As previously mentioned, we found that larger AEs have larger stress-drops. It is worth mentioning that several factors might bias our estimates of AE stress-drop. First, the source model (Equation 10) we use assumes that attenuation,  $Q$ , is frequency independent. Ide et al. (2003) used a Boatwright source model (Boatwright, 1978) with a constant  $Q$  to estimate the stress-drops of a set of microearthquakes recorded in a borehole in California and compared their results with the stress-drops estimated by spectral ratio. The authors showed that the assumption of  $Q$  frequency independent leads to a systematic underestimation of stress-drop, particularly for the small events. Similar observations were made by Kwiitek, Bulut, et al. (2014). Second, the acoustic sensors used in the experiments record in a limited frequency band. Therefore, corner frequencies close to the upper bandwidth limit are likely to be biased (Abercrombie, 2015; Ruhl et al., 2017). However, this seems unlikely because the sensors' response is characterized by a resonance band between 1.2 and 2.2 MHz (Figure 2) while the upper limit of the estimated corner frequencies is  $\sim 1.5$  MHz (Figure 4). At last, the increase in stress-drop with AE size might be related to insufficiently well calibrated acoustic sensors. The use of Empirical Green Function (i.e., EGF) approaches (Abercrombie et al., 2016; Shearer et al., 2019) to estimate the AE stress-drops would certainly improve the reliability of the measurements but is beyond the scope of this study. Despite the uncertainties in stress-drop measurements, the increase in stress-drop with AE size might still be informative and physically meaningful. Large foreshocks tend to occur closer to stick-slip instability, when the weakening rate is faster due to accelerating slip, which thus may result in larger stress-drops. Assuming that foreshocks highlight the rupture of locked and critically stressed asperities, these asperities become increasingly seismic as fault slip accelerates. This is consistent with observations at the scale of crustal faults. Bouchon et al. (2013) showed that foreshock sequences were more common for interplate than for intraplate earthquakes due to facilitating slow slip phase at plate boundaries. Similarly, McGuire et al. (2005) have observed that oceanic transform faults with relatively high-slip rates were producing more foreshock sequences.

Extending the scaling relationship between  $M_{0a}$  and  $M_{0p}$  (Figure 10a) to larger pre-seismic moments would rapidly lead to 100% of seismic coupling. Fixing  $n = 4$  and taking the experiment conducted at  $P_c = 45$  MPa as an example,  $M_{0a}$  would equal  $M_{0p}$  for  $M_{0p} \approx 10^{4.5}$  N.m which is equivalent to an amount of pre-slip of about 300  $\mu$ m. If we assume a ratio of  $M_{0p}/M_{0c}$  of about 5%, 300  $\mu$ m of pre-slip gives 6 mm of coseismic displacement which is a typical value for a magnitude 2.5–3 earthquake. Tamaribuchi et al. (2018) analyzed foreshock(s)-mainshock-aftershock(s) sequences in the JMA catalog over a 20-year period. The authors found that the magnitude of the largest foreshock within a sequence scales with the magnitude of the mainshock but numerous mainshocks are not preceded by foreshocks (at least not by foreshocks of  $M_w > 1.0$ , the completeness magnitude of the catalog) and, when they do, it is common that the largest foreshock is at least two orders of moment magnitude less than that of the mainshock. Therefore, the extrapolation of the scaling relationship we find between  $M_{0a}$  and  $M_{0p}$  to a larger scale is likely to be invalid. Indeed, in addition to be dictated by the way mainshocks initiate in our experiments, the relationship between  $M_{0a}$  and  $M_{0p}$  is likely to be controlled by the actual experimental conditions: a constant fault surface, a rapid loading which prevents healing and a smooth planar fault with a low degree of structural complexity (damage zone, fault branches, lithology contrast to cite only a few). Nevertheless, our observations suggest that valuable insights on earthquake nucleation mode, in a specific geological context, can be obtained by examining the relationship between  $M_{0a}$  and  $M_{0p}$ .

Although the nucleation phase is difficult to image using geodetic measurements, recent observations on well instrumented earthquakes constitute exceptions. The pre-seismic moment was estimated using geodetic for the 2011  $M_w$  9.0 Tohoku-Oki earthquake (Kato et al., 2012), the 2012  $M_w$  7.6 Nicoya earthquake (Voss et al., 2018), the 2014  $M_w$  8.2 Iquique earthquake (Socquet et al., 2017) and the 2015  $M_w$  8.4 Illapel earthquake (Huang & Meng, 2018). For these earthquakes,  $M_{0p}/M_{0c}$  ranges from about 0.4% to 3% which is very close to our estimates (4%, 6%, and 2% of at  $P_c = 30, 45$ , and 60 MPa respectively). Different forms of Equation 21 were proposed, for

instance the one proposed by Acosta et al. (2019b), as previously mentioned, or the well-known one  $M_{0p} \propto M_{0c}^{0.78}$  proposed by Abercrombie and Rice (2005) within the framework of slip-weakening theory and on the basis of seismological observations. Our data alone do not allow us to state on the scaling exponent of Equation 21 but by comparing data from experimental and natural earthquakes, fracture energy must be proportional to co-seismic displacement (i.e.,  $M_{0p} \propto M_{0c}$ ) for  $M_{0p}/M_{0c}$  to be of the same order over such a large range of moment magnitudes. It is likely that the improvements currently made in seismic/geodetic instrumentation and data processing techniques will make possible to estimate  $M_{0p}/M_{0c}$  for a large range of moment magnitudes and thereby will bring new insights to Equation 21.

Comparing the total foreshock moment release  $M_{0a}$  with the co-seismic moment release  $M_{0p}$  in our experiments, there is up to seven orders of magnitude difference between  $M_{0a}$  and  $M_{0c}$ , or equivalently four orders of magnitude difference in terms of moment magnitude  $M_w$ . At the crustal scale, a case study is the one of the 1,999  $M_w$  7.6 Izmit earthquake. While the nucleation of the 1999 Izmit earthquake is still debated (i.e., cascade model W. L. Ellsworth and Bulut (2018), or preslip model Bouchon et al. (2011, 2021)), Bouchon et al. (2011) inferred the precursory moment  $M_w$  7.6 Izmit earthquake from a sequence of repeaters which occurred within the last hour prior to the mainshock. The authors argued that the occurrence of repeaters required a fast reloading of stress and, thereby, manifested the expansion of a nucleation patch. Bouchon et al. (2011) estimated the pre-seismic moment to be six orders of magnitude smaller than the co-seismic moment, a ratio abnormally low. However, our data show that seismic coupling may be very low during nucleation and, consequently, that a strict equality between seismic moment released by repeaters and pre-seismic moment is questionable. The seismic moment released by repeaters should be interpreted as the smallest possible value of  $M_{0p}$ . Moreover, our observations question the parallel commonly drawn between a lack of detectable seismicity prior to a mainshock and a cascading process. Nucleation process could be too silent in some cases for the nucleation phase to be detected by seismic instruments. Indeed, similar experiments, performed under fluid saturated conditions, led to the absence of detectable foreshock sequences (Acosta et al., 2019a), although mainshocks were preceded by a long slow-slip transients.

Finally, foreshock migration toward mainshock hypocenter is generally attributed to slow-slip propagation (Kato & Nakagawa, 2014; Kato et al., 2012; Kato, Fukuda, Nakagawa, & Obara, 2016; Ruiz et al., 2014), stress-transfer (static or dynamic, W. L. Ellsworth and Bulut (2018); Yao et al. (2020)) or fluid diffusion (Moreno et al., 2015; Socquet et al., 2017). Here, we proposed an alternative explanation, rarely considered yet theoretically predicted, which is that foreshock migration arises from slip localization, promoted by a rapid weakening rate, onto a fault patch. In practice, foreshock migration due to slip localization would be easily distinguishable from foreshock migration due to fluid diffusion or to slow-slip propagation since fluid-diffusion driven foreshocks migrate as the square root of time, and slow-slip driven foreshocks migrate as slip lines. The question whether slow-slip transients prior to large earthquakes are part of the nucleation process is still debated. As an example, the 2011  $M_w$  9.0 Tohoku-oki earthquake was preceded by slow-slip events but the latter did not propagate with slip (and foreshock rate) acceleration which is kinematically expected in case of a nucleation process. Foreshock migration due to stress-transfer or slip localization share similar spatio-temporal characteristics. To distinguish one from another would require strong constraints on foreshocks size, magnitude and location, provided that foreshock sequence does not stem from the feedback between the two processes as evidenced by the present study and previous experimental works (McLaskey & Lockner, 2014; Passelègue et al., 2017; Yamashita et al., 2021) and numerical simulations (Cattania & Segall, 2021).

## 7. Conclusions

In this study, we recorded microseismicity generated during stick-slip experiments and analyzed the spatio-temporal dynamics of precursory foreshocks and slip prior to stick-slip instabilities. Using calibrated acoustic sensors, foreshock source parameters were also determined. Our results evidence that the occurrence of foreshocks was driven by fault slip acceleration during the nucleation phase of the upcoming stick-slip instability. Figure 11 summarizes the dynamics of the nucleation phase, during which:

1. Pre-slip on the entire fault was systematically observed preceding failure. Much in agreement with the pioneering work of Dieterich (1992), slip and stress heterogeneities result in slip localization onto a patch of the fault, which is reflected by foreshock migration toward the epicenter, and a decrease of the  $b$ -value from  $\sim 1$  to  $\sim 0.5$ .
2. The foreshock rate is driven by slip velocity. As slip accelerates, so does the foreshock rate, which increases as an inverse Omori-law. An experimental scaling with the nucleation size was found experimentally for

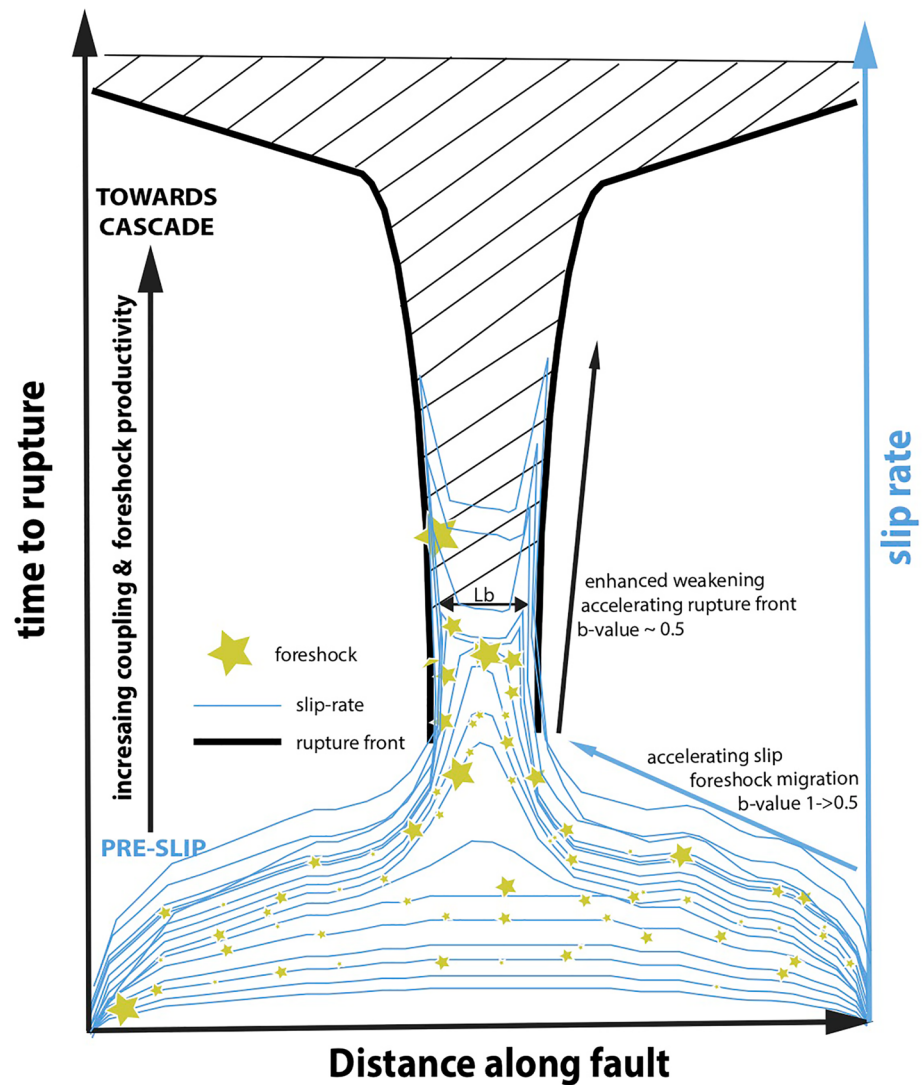


**Figure 11.** Schematics of nucleation phase dynamics. Slip and stress heterogeneities result in slip localization onto a patch of the fault, which is reflected by foreshock migration toward the epicenter. At  $t = c$  of the inverse Omori-law, we observe the transition from a frictional, “Dieterich-like” (Dieterich, 1992), instability, to that of a fracture, “Ohnaka-like” (Ohnaka, 2003), process.

- the inverse Omori-law, which suggest that indeed, foreshocks are driven by a nucleation process of given length-scale.
3. As the fault accelerates, the nucleation size shrinks because of enhanced slip and velocity weakening. At  $t = c$  of the inverse Omori-law, the nucleation size has shrunk enough (or strain has localized enough, or the weakening rate is fast enough), that we observe the transition from a frictional, “Dieterich-like” (Dieterich, 1992), instability, to that of a fracture, “Ohnaka-like” (Ohnaka, 2003), process.
  4. From the ratio between the seismic and the aseismic components of the nucleation phase, we find that this transition from “slip to crack” also corresponds to the transition between the nucleation phase being almost fully aseismic, toward a cascading process. The question remains opened however on whether the mainshock is truly triggered by a cascade-like process, that is, whether the mainshock is a foreshock that degenerates by rupturing a patch large—or weak—enough to propagate over the entire fault plane. Recent seismological observations of the self-similarity between small and large earthquakes (Ide, 2019) suggest it could indeed be the case.



## Conflict of Interest

The authors declare no conflicts of interest relevant to this study.

## Data Availability Statement

All data are available online at: <https://doi.org/10.4121/22261660.v1>.

## Acknowledgments

This work was funded by the European Research Council grant REALISM (2016-Grant 681346). H. S. B. acknowledges the European Research Council grant PERSISMO (Grant 865411) for partial support of this work.

## References

- Abercrombie, R. E. (1995). Earthquake source scaling relationships from 1 to 5 ml using seismograms recorded at 2.5-km depth. *Journal of Geophysical Research*, 100(B12), 24015–24036. <https://doi.org/10.1029/95jb02397>
- Abercrombie, R. E. (2015). Investigating uncertainties in empirical green's function analysis of earthquake source parameters. *Journal of Geophysical Research: Solid Earth*, 120(6), 4263–4277. <https://doi.org/10.1002/2015jb011984>
- Abercrombie, R. E., Bannister, S., Ristau, J., & Doser, D. (2016). Variability of earthquake stress drop in a subduction setting, the hikurangi margin, New Zealand. *Geophysical Journal International*, 208(1), ggw393. <https://doi.org/10.1093/gji/ggw393>
- Abercrombie, R. E., & Mori, J. (1996). Occurrence patterns of foreshocks to large earthquakes in the western United States. *Nature*, 381(6580), 303–307. <https://doi.org/10.1038/381303a0>
- Abercrombie, R. E., & Rice, J. R. (2005). Can observations of earthquake scaling constrain slip weakening? *Geophysical Journal International*, 162(2), 406–424. <https://doi.org/10.1111/j.1365-246x.2005.02579.x>
- Acosta, M., Passelègue, F. X., Schubnel, A., Madariaga, R., & Violay, M. (2019a). Can precursory moment release scale with earthquake magnitude? A view from the laboratory. *Geophysical Research Letters*, 46(22), 12927–12937. <https://doi.org/10.1029/2019gl084744>
- Acosta, M., Passelègue, F. X., Schubnel, A., Madariaga, R., & Violay, M. (2019b). Precursory moment release scales with earthquake magnitude. *arXiv preprint*. arXiv:1901.06908.
- Aki, K. (1967). Scaling law of seismic spectrum. *Journal of Geophysical Research*, 72(4), 1217–1231. <https://doi.org/10.1029/jz072i004p01217>
- Aki, K. (1981). A probabilistic synthesis of precursory phenomena. *Earthquake prediction: an international review*, 4, 566–574.
- Aki, K., & Richards, P. G. (2002). Quantitative seismology.
- Ampuero, J.-P., & Rubin, A. M. (2008). Earthquake nucleation on rate and state faults—aging and slip laws. *Journal of Geophysical Research*, 113(B1), B01302. <https://doi.org/10.1029/2007jb005082>
- Aubry, J., Passelègue, F., Escartin, J., Gasc, J., Deldicque, D., & Schubnel, A. (2020). Fault stability across the seismogenic zone. *Journal of Geophysical Research: Solid Earth*, 125(8), e2020JB019670. <https://doi.org/10.1029/2020jb019670>
- Beroza, G. C., & Ellsworth, W. L. (1996). Properties of the seismic nucleation phase. *Tectonophysics*, 261(1–3), 209–227. [https://doi.org/10.1016/0040-1951\(96\)00067-4](https://doi.org/10.1016/0040-1951(96)00067-4)
- Blanke, A., Kwiatek, G., Goebel, T. H., Bohnhoff, M., & Dresen, G. (2021). Stress drop—magnitude dependence of acoustic emissions during laboratory stick-slip. *Geophysical Journal International*, 224(2), 1371–1380. <https://doi.org/10.1093/gji/ggaa524>
- Boatwright, J. (1978). Detailed spectral analysis of two small New York state earthquakes. *Bulletin of the Seismological Society of America*, 68(4), 1117–1131.
- Bouchon, M., Durand, V., Marsan, D., Karabulut, H., & Schmittbuhl, J. (2013). The long precursory phase of most large interplate earthquakes. *Nature Geoscience*, 6(4), 299–302. <https://doi.org/10.1038/ngeo1770>
- Bouchon, M., Karabulut, H., Aktar, M., Özalaybey, S., Schmittbuhl, J., & Bouin, M.-P. (2011). Extended nucleation of the 1999  $M_w$  7.6 Izmit earthquake. *Science*, 331(6019), 877–880. <https://doi.org/10.1126/science.1197341>
- Bouchon, M., Karabulut, H., Aktar, M., Özalaybey, S., Schmittbuhl, J., Bouin, M.-P., & Marsan, D. (2021). The nucleation of the Izmit and Düzce earthquakes: Some mechanical logic on where and how ruptures began. *Geophysical Journal International*, 225(3), 1510–1517. <https://doi.org/10.1093/gji/ggab040>
- Brantut, N., Schubnel, A., & Guéguen, Y. (2011). Damage and rupture dynamics at the brittle-ductile transition: The case of gypsum. *Journal of Geophysical Research*, 116(B1), B01404. <https://doi.org/10.1029/2010jb007675>
- Campillo, M., & Ionescu, I. R. (1997). Initiation of antiplane shear instability under slip dependent friction. *Journal of Geophysical Research*, 102(B9), 20363–20371. <https://doi.org/10.1029/97jb01508>
- Cattania, C., & Segall, P. (2021). Precursory slow slip and foreshocks on rough faults. *Journal of Geophysical Research: Solid Earth*, 126(4), e2020JB020430. <https://doi.org/10.1029/2020jb020430>
- Cocco, M., Tinti, E., Marone, C., & Piatanesi, A. (2009). Scaling of slip weakening distance with final slip during dynamic earthquake rupture. *International Geophysics*, 94, 163–186. [https://doi.org/10.1016/S0074-6142\(08\)00007-7](https://doi.org/10.1016/S0074-6142(08)00007-7)
- Dieterich, J. H. (1992). Earthquake nucleation on faults with rate-and state-dependent strength. *Tectonophysics*, 211(1–4), 115–134. [https://doi.org/10.1016/0040-1951\(92\)90055-b](https://doi.org/10.1016/0040-1951(92)90055-b)
- Di Toro, G., Han, R., Hirose, T., De Paola, N., Nielsen, S., Mizoguchi, K., et al. (2011). Fault lubrication during earthquakes. *Nature*, 471(7339), 494–498. <https://doi.org/10.1038/nature09838>
- Ellsworth, W. L., & Beroza, G. (1995). Seismic evidence for an earthquake nucleation phase. *Science*, 268(5212), 851–855. <https://doi.org/10.1126/science.268.5212.851>
- Ellsworth, W. L., & Bulut, F. (2018). Nucleation of the 1999 Izmit earthquake by a triggered cascade of foreshocks. *Nature Geoscience*, 11(7), 531–535. <https://doi.org/10.1038/s41561-018-0145-1>
- Enescu, B., & Ito, K. (2001). Some premonitory phenomena of the 1995 Hyogo-Ken Nanbu (Kobe) earthquake: Seismicity, b-value and fractal dimension. *Tectonophysics*, 338(3–4), 297–314. [https://doi.org/10.1016/S0040-1951\(01\)00085-3](https://doi.org/10.1016/S0040-1951(01)00085-3)
- Eshelby, J. D. (1957). The determination of the elastic field of an ellipsoidal inclusion, and related problems. *Proceedings of the Royal Society of London Series A. Mathematical and Physical Sciences*, 241(1226), 376–396.
- Fang, Z., Dieterich, J. H., & Xu, G. (2010). Effect of initial conditions and loading path on earthquake nucleation. *Journal of Geophysical Research*, 115(B6), B06313. <https://doi.org/10.1029/2009jb006558>
- Fukuyama, E., Tsuchida, K., Kawakata, H., Yamashita, F., Mizoguchi, K., & Xu, S. (2018). Spatiotemporal complexity of 2-D rupture nucleation observed by direct monitoring during large-scale biaxial rock friction experiments. *Tectonophysics*, 733, 182–192. <https://doi.org/10.1016/j.tecto.2017.12.023>



- Goebel, T., Becker, T., Schorlemmer, D., Stanchits, S., Sammis, C., Rybacki, E., & Dresen, G. (2012). Identifying fault heterogeneity through mapping spatial anomalies in acoustic emission statistics. *Journal of Geophysical Research*, 117(B3), B03310. <https://doi.org/10.1029/2011jb008763>
- Goebel, T., Schorlemmer, D., Becker, T., Dresen, G., & Sammis, C. (2013). Acoustic emissions document stress changes over many seismic cycles in stick-slip experiments. *Geophysical Research Letters*, 40(10), 2049–2054. <https://doi.org/10.1002/grl.50507>
- Goldberg, D., Badri, M., & Wepfer, W. (1992). Acoustic attenuation in oceanic gabbro. *Geophysical Journal International*, 111(2), 193–202. <https://doi.org/10.1111/j.1365-246x.1992.tb00569.x>
- Goldsby, D. L., & Tullis, T. E. (2011). Flash heating leads to low frictional strength of crustal rocks at earthquake slip rates. *Science*, 334(6053), 216–218. <https://doi.org/10.1126/science.1207902>
- Gounon, A., Latour, S., Letort, J., & El Arem, S. (2022). Rupture nucleation on a periodically heterogeneous interface. *Geophysical Research Letters*, 49(20), e2021GL096816. <https://doi.org/10.1029/2021gl096816>
- Guérin-Marthe, S., Nielsen, S., Bird, R., Giani, S., & Di Toro, G. (2019). Earthquake nucleation size: Evidence of loading rate dependence in laboratory faults. *Journal of Geophysical Research: Solid Earth*, 124(1), 689–708. <https://doi.org/10.1029/2018jb016803>
- Gvirtzman, S., & Fineberg, J. (2021). Nucleation fronts ignite the interface rupture that initiates frictional motion. *Nature Physics*, 17(9), 1037–1042. <https://doi.org/10.1038/s41567-021-01299-9>
- Harbord, C. W., Nielsen, S. B., De Paola, N., & Holdsworth, R. E. (2017). Earthquake nucleation on rough faults. *Geology*, 45(10), 931–934. <https://doi.org/10.1130/g39181.1>
- Helmstetter, A., & Sornette, D. (2003). Foreshocks explained by cascades of triggered seismicity. *Journal of Geophysical Research*, 108(B10), 2457. <https://doi.org/10.1029/2003jb002409>
- Hiramatsu, Y., Yamanaka, H., Tadokoro, K., Nishigami, K. y., & Ohmi, S. (2002). Scaling law between corner frequency and seismic moment of microearthquakes: Is the breakdown of the cube law a nature of earthquakes? *Geophysical Research Letters*, 29(8), 52–54. <https://doi.org/10.1029/2001gl013894>
- Huang, H., & Meng, L. (2018). Slow unlocking processes preceding the 2015 Mw 8.4 Illapel, Chile, earthquake. *Geophysical Research Letters*, 45(9), 3914–3922. <https://doi.org/10.1029/2018gl077060>
- Ida, Y. (1972). Cohesive force across the tip of a longitudinal-shear crack and Griffith's specific surface energy. *Journal of Geophysical Research*, 77(20), 3796–3805. <https://doi.org/10.1029/jb077i020p03796>
- Ide, S. (2019). Frequent observations of identical onsets of large and small earthquakes. *Nature*, 573(7772), 112–116. <https://doi.org/10.1038/s41586-019-1508-5>
- Ide, S., Beroza, G. C., Prejean, S. G., & Ellsworth, W. L. (2003). Apparent break in earthquake scaling due to path and site effects on deep borehole recordings. *Journal of Geophysical Research*, 108(B5), 2271. <https://doi.org/10.1029/2001jb001617>
- Ide, S., & Takeo, M. (1997). Determination of constitutive relations of fault slip based on seismic wave analysis. *Journal of Geophysical Research*, 102(B12), 27379–27391. <https://doi.org/10.1029/97jb02675>
- Johnson, P. A., Rouet-Leduc, B., Pyrak-Nolte, L. J., Beroza, G. C., Marone, C. J., Hulbert, C., et al. (2021). Laboratory earthquake forecasting: A machine learning competition. *Proceedings of the National Academy of Sciences*, 118(5), e2011362118. <https://doi.org/10.1073/pnas.2011362118>
- Jones, L., & Molnar, P. (1976). Frequency of foreshocks. *Nature*, 262(5570), 677–679. <https://doi.org/10.1038/262677a0>
- Jones, L. M., & Molnar, P. (1979). Some characteristics of foreshocks and their possible relationship to earthquake prediction and premonitory slip on faults. *Journal of Geophysical Research*, 84(B7), 3596–3608. <https://doi.org/10.1029/jb084ib07p03596>
- Kaneko, Y., & Lapusta, N. (2008). Variability of earthquake nucleation in continuum models of rate-and-state faults and implications for after-shock rates. *Journal of Geophysical Research*, 113(B12), B12312. <https://doi.org/10.1029/2007jb005154>
- Kato, A., Fukuda, J., Kumazawa, T., & Nakagawa, S. (2016). Accelerated nucleation of the 2014 Iquique, Chile  $M_w$  8.2 earthquake. *Scientific Reports*, 6(1), 24792. <https://doi.org/10.1038/srep24792>
- Kato, A., Fukuda, J., Nakagawa, S., & Obara, K. (2016). Foreshock migration preceding the 2016  $M_w$  7.0 Kumamoto earthquake, Japan. *Geophysical Research Letters*, 43(17), 8945–8953. <https://doi.org/10.1002/2016gl070079>
- Kato, A., & Nakagawa, S. (2014). Multiple slow-slip events during a foreshock sequence of the 2014 Iquique, Chile  $M_w$  8.1 earthquake. *Geophysical Research Letters*, 41(15), 5420–5427. <https://doi.org/10.1002/2014gl061138>
- Kato, A., Obara, K., Igarashi, T., Tsuruoka, H., Nakagawa, S., & Hirata, N. (2012). Propagation of slow slip leading up to the 2011  $M_w$  9.0 Tohoku-Oki earthquake. *Science*, 335(6069), 705–708. <https://doi.org/10.1126/science.1215141>
- Kwiatek, G., Bulut, F., Bohnhoff, M., & Dresen, G. (2014). High-resolution analysis of seismicity induced at berlín geothermal field, El Salvador. *Geothermics*, 52, 98–111. <https://doi.org/10.1016/j.geothermics.2013.09.008>
- Kwiatek, G., Goebel, T., & Dresen, G. (2014). Seismic moment tensor and  $b$  value variations over successive seismic cycles in laboratory stick-slip experiments. *Geophysical Research Letters*, 41(16), 5838–5846. <https://doi.org/10.1002/2014gl060159>
- Kwiatek, G., Plenkens, K., Dresen, G., & Group, J. R. (2011). Source parameters of picoseismicity recorded at mponeng deep gold mine, South Africa: Implications for scaling relations. *Bulletin of the Seismological Society of America*, 101(6), 2592–2608. <https://doi.org/10.1785/0120110094>
- Lapusta, N., & Rice, J. R. (2003). Nucleation and early seismic propagation of small and large events in a crustal earthquake model. *Journal of Geophysical Research*, 108(B4), B05311. <https://doi.org/10.1029/2001jb000793>
- Latour, S., Schubnel, A., Nielsen, S., Madariaga, R., & Vinciguerra, S. (2013). Characterization of nucleation during laboratory earthquakes. *Geophysical Research Letters*, 40(19), 5064–5069. <https://doi.org/10.1002/grl.50974>
- Lebihain, M., Roch, T., Violay, M., & Molinari, J.-F. (2021). Earthquake nucleation along faults with heterogeneous weakening rate. *Geophysical Research Letters*, 48(21), e2021GL094901. <https://doi.org/10.1029/2021gl094901>
- Lei, X., Li, S., & Liu, L. (2018). Seismic  $b$ -value for foreshock ae events preceding repeated stick-slips of pre-cut faults in granite. *Applied Sciences*, 8(12), 2361. <https://doi.org/10.3390/app8122361>
- Liu, C., & Ahrens, T. J. (1997). Stress wave attenuation in shock-damaged rock. *Journal of Geophysical Research*, 102(B3), 5243–5250. <https://doi.org/10.1029/96jb03891>
- Lockner, D. (1993). The role of acoustic emission in the study of rock fracture. In *International journal of rock mechanics and mining sciences & geomechanics abstracts* (Vol. 30, pp. 883–899).
- Lockner, D., Byerlee, J., Kuksenko, V., Ponomarev, A., & Sidorin, A. (1991). Quasi-static fault growth and shear fracture energy in granite. *Nature*, 350(6313), 39–42. <https://doi.org/10.1038/350039a0>
- Madariaga, R. (1976). Dynamics of an expanding circular fault. *Bulletin of the Seismological Society of America*, 66(3), 639–666. <https://doi.org/10.1785/bssa0660030639>

- Main, I. G., Meredith, P. G., & Jones, C. (1989). A reinterpretation of the precursory seismic *b*-value anomaly from fracture mechanics. *Geophysical Journal International*, 96(1), 131–138. <https://doi.org/10.1111/j.1365-246x.1989.tb05255.x>
- Marone, C. (1998). Laboratory-derived friction laws and their application to seismic faulting. *Annual Review of Earth and Planetary Sciences*, 26(1), 643–696. <https://doi.org/10.1146/annurev.earth.26.1.643>
- Marsan, D., Helmstetter, A., Bouchon, M., & Dublanchet, P. (2014). Foreshock activity related to enhanced aftershock production. *Geophysical Research Letters*, 41(19), 6652–6658. <https://doi.org/10.1002/2014gl012119>
- McGuire, J. J., Boettcher, M. S., & Jordan, T. H. (2005). Foreshock sequences and short-term earthquake predictability on east Pacific rise transform faults. *Nature*, 434(7032), 457–461. <https://doi.org/10.1038/nature03377>
- McLaskey, G. C. (2019). Earthquake initiation from laboratory observations and implications for foreshocks. *Journal of Geophysical Research: Solid Earth*, 124(12), 12882–12904. <https://doi.org/10.1029/2019jb018363>
- McLaskey, G. C., & Kilgore, B. D. (2013). Foreshocks during the nucleation of stick-slip instability. *Journal of Geophysical Research: Solid Earth*, 118(6), 2982–2997. <https://doi.org/10.1002/jgrb.50232>
- McLaskey, G. C., & Lockner, D. A. (2014). Preslip and cascade processes initiating laboratory stick slip. *Journal of Geophysical Research: Solid Earth*, 119(8), 6323–6336. <https://doi.org/10.1002/2014jb011220>
- Moreno, M., Li, S., Angiboust, S., Schurr, B., Bedford, J., & Oncken, O. (2015). The 2014 Iquique Chile earthquake: Preparatory breaking processes of a locked asperity and natural constraints for fluid migration along the plate interface. In *Agü fall meeting abstracts*.
- Nanjo, K., Hirata, N., Obara, K., & Kasahara, K. (2012). Decade-scale decrease in *b* value prior to the M9-class 2011 Tohoku and 2004 Sumatra quakes. *Geophysical Research Letters*, 39(20), L20304. <https://doi.org/10.1029/2012gl052997>
- Narteau, C., Byrdina, S., Shebalin, P., & Schorlemmer, D. (2009). Common dependence on stress for the two fundamental laws of statistical seismology. *Nature*, 462(7273), 642–645. <https://doi.org/10.1038/nature08553>
- Narteau, C., Shebalin, P., & Holschneider, M. (2002). Temporal limits of the power law aftershock decay rate. *Journal of Geophysical Research*, 107(B12), ESE-12. <https://doi.org/10.1029/2002jb001868>
- Nielsen, S., Taddeucci, J., & Vinciguerra, S. (2010). Experimental observation of stick-slip instability fronts. *Geophysical Journal International*, 180(2), 697–702. <https://doi.org/10.1111/j.1365-246x.2009.04444.x>
- Ogata, Y. (1983). Estimation of the parameters in the modified omori formula for aftershock frequencies by the maximum likelihood procedure. *Journal of Physics of the Earth*, 31(2), 115–124. <https://doi.org/10.4294/jpe1952.31.115>
- Ogata, Y. (1988). Statistical models for earthquake occurrences and residual analysis for point processes. *Journal of the American Statistical Association*, 83(401), 9–27. <https://doi.org/10.1080/01621459.1988.10478560>
- Ohnaka, M. (1992). Earthquake source nucleation: A physical model for short-term precursors. *Tectonophysics*, 211(1–4), 149–178. [https://doi.org/10.1016/0040-1951\(92\)90057-d](https://doi.org/10.1016/0040-1951(92)90057-d)
- Ohnaka, M. (2003). A constitutive scaling law and a unified comprehension for frictional slip failure, shear fracture of intact rock, and earthquake rupture. *Journal of Geophysical Research*, 108(B2), 2080. <https://doi.org/10.1029/2000jb000123>
- Ohnaka, M. (2013). *The physics of rock failure and earthquakes*. Cambridge University Press.
- Ohnaka, M., & Kuwahara, Y. (1990). Characteristic features of local breakdown near a crack-tip in the transition zone from nucleation to unstable rupture during stick-slip shear failure. *Tectonophysics*, 175(1–3), 197–220. [https://doi.org/10.1016/0040-1951\(90\)90138-x](https://doi.org/10.1016/0040-1951(90)90138-x)
- Ojala, I. O., Main, I. G., & Ngwenya, B. T. (2004). Strain rate and temperature dependence of Omori law scaling constants of AE data: Implications for earthquake foreshock-aftershock sequences. *Geophysical Research Letters*, 31(24), L24617. <https://doi.org/10.1029/2004gl020781>
- Okubo, P. G., & Dieterich, J. H. (1984). Effects of physical fault properties on frictional instabilities produced on simulated faults. *Journal of Geophysical Research*, 89(B7), 5817–5827. <https://doi.org/10.1029/jb089ib07p05817>
- Olsen, K., Madariaga, R., & Archuleta, R. J. (1997). Three-dimensional dynamic simulation of the 1992 Landers earthquake. *Science*, 278(5339), 834–838. <https://doi.org/10.1126/science.278.5339.834>
- Papazachos, B. C. (1973). The time distribution of the reservoir-associated foreshocks and its importance to the prediction of the principal shock. *Bulletin of the Seismological Society of America*, 63(6–1), 1973–1978. <https://doi.org/10.1785/bssa0636-11973>
- Passelègue, F. X., Latour, S., Schubnel, A., Nielsen, S., Bhat, H. S., & Madariaga, R. (2017). Influence of fault strength on precursory processes during laboratory earthquakes. In *Fault zone dynamic processes: Evolution of fault properties during seismic rupture* (Vol. 227, p. 229).
- Passelègue, F. X., Schubnel, A., Nielsen, S., Bhat, H. S., Deldicque, D., & Madariaga, R. (2016). Dynamic rupture processes inferred from laboratory microearthquakes. *Journal of Geophysical Research: Solid Earth*, 121(6), 4343–4365. <https://doi.org/10.1002/2015jb012694>
- Prieto, G. A., Shearer, P. M., Vernon, F. L., & Kilb, D. (2004). Earthquake source scaling and self-similarity estimation from stacking P and S spectra. *Journal of Geophysical Research*, 109(B8), B08310. <https://doi.org/10.1029/2004jb003084>
- Rice, J. R. (2006). Heating and weakening of faults during earthquake slip. *Journal of Geophysical Research*, 111(B5), B05311. <https://doi.org/10.1029/2005jb004006>
- Rivière, J., Lv, Z., Johnson, P., & Marone, C. (2018). Evolution of *b*-value during the seismic cycle: Insights from laboratory experiments on simulated faults. *Earth and Planetary Science Letters*, 482, 407–413. <https://doi.org/10.1016/j.epsl.2017.11.036>
- Rubin, A. M., & Ampuero, J.-P. (2005). Earthquake nucleation on (aging) rate and state faults. *Journal of Geophysical Research*, 110(B11), B11312. <https://doi.org/10.1029/2005jb003686>
- Ruhl, C., Abercrombie, R., & Smith, K. (2017). Spatiotemporal variation of stress drop during the 2008 Mogul, Nevada, earthquake swarm. *Journal of Geophysical Research: Solid Earth*, 122(10), 8163–8180. <https://doi.org/10.1002/2017jb014601>
- Ruiz, S., Metois, M., Fuenzalida, A., Ruiz, J., Leyton, F., Grandin, R., et al. (2014). Intense foreshocks and a slow slip event preceded the 2014 Iquique  $M_w$  8.1 earthquake. *Science*, 345(6201), 1165–1169. <https://doi.org/10.1126/science.1256074>
- Sammonds, P., Meredith, P., & Main, I. (1992). Role of pore fluids in the generation of seismic precursors to shear fracture. *Nature*, 359(6392), 228–230. <https://doi.org/10.1038/359228a0>
- Schär, S., Albertini, G., & Kammer, D. S. (2021). Nucleation of frictional sliding by coalescence of microslip. *International Journal of Solids and Structures*, 225, 111059. <https://doi.org/10.1016/j.ijsolstr.2021.111059>
- Scholz, C. (1968). The frequency-magnitude relation of microfracturing in rock and its relation to earthquakes. *Bulletin of the Seismological Society of America*, 58(1), 399–415. <https://doi.org/10.1785/bssa0580010399>
- Schubnel, A., Fortin, J., Burlini, L., & Gueguen, Y. (2005). Damage and recovery of calcite rocks deformed in the cataclastic regime. *Geological Society, London, Special Publications*, 245(1), 203–221. <https://doi.org/10.1144/gsl.sp.2005.245.01.10>
- Schubnel, A., Thompson, B., Fortin, J., Guéguen, Y., & Young, R. (2007). Fluid-induced rupture experiment on Fontainebleau sandstone: Premonitory activity, rupture propagation, and aftershocks. *Geophysical Research Letters*, 34(19), L19307. <https://doi.org/10.1029/2007gl031076>
- Selvadurai, P. A. (2019). Laboratory insight into seismic estimates of energy partitioning during dynamic rupture: An observable scaling breakdown. *Journal of Geophysical Research: Solid Earth*, 124(11), 11350–11379. <https://doi.org/10.1029/2018jb017194>

- Selvadurai, P. A., & Glaser, S. D. (2015). Laboratory-developed contact models controlling instability on frictional faults. *Journal of Geophysical Research: Solid Earth*, 120(6), 4208–4236. <https://doi.org/10.1002/2014jb011690>
- Shearer, P. M., Abercrombie, R. E., Trugman, D. T., & Wang, W. (2019). Comparing EGF methods for estimating corner frequency and stress drop from p wave spectra. *Journal of Geophysical Research: Solid Earth*, 124(4), 3966–3986. <https://doi.org/10.1029/2018jb016957>
- Shearer, P. M., Meng, H., & Fan, W. (2022). Earthquake detection using a nodal array on the San Jacinto fault in California: Evidence for high foreshock rates preceding many events. *Journal of Geophysical Research: Solid Earth*, 128(3), e2022JB025279. <https://doi.org/10.1029/2022JB025279>
- Socquet, A., Valdes, J. P., Jara, J., Cotton, F., Walpersdorf, A., Cotte, N., et al. (2017). An 8 month slow slip event triggers progressive nucleation of the 2014 Chile megathrust. *Geophysical Research Letters*, 44(9), 4046–4053. <https://doi.org/10.1002/2017gl073023>
- Suyehiro, S. (1966). Difference between aftershocks and foreshocks in the relationship of magnitude to frequency of occurrence for the great Chilean earthquake of 1960. *Bulletin of the Seismological Society of America*, 56(1), 185–200. <https://doi.org/10.1785/bssa0560010185>
- Tamaribuch, K., Yagi, Y., Enescu, B., & Hirano, S. (2018). Characteristics of foreshock activity inferred from the JMA earthquake catalog. *Earth Planets and Space*, 70(1), 90. <https://doi.org/10.1186/s40623-018-0866-9>
- Thompson, B., Young, R., & Lockner, D. A. (2009). Premonitory acoustic emissions and stick-slip in natural and smooth-faulted westerly granite. *Journal of Geophysical Research*, 114(B2), B02205. <https://doi.org/10.1029/2008jb005753>
- Tinti, E., Cocco, M., Fukuyama, E., & Piatanesi, A. (2009). Dependence of slip weakening distance ( $d_c$ ) on final slip during dynamic rupture of earthquakes. *Geophysical Journal International*, 177(3), 1205–1220. <https://doi.org/10.1111/j.1365-246x.2009.04143.x>
- Tormann, T., Enescu, B., Woessner, J., & Wiemer, S. (2015). Randomness of megathrust earthquakes implied by rapid stress recovery after the Japan earthquake. *Nature Geoscience*, 8(2), 152–158. <https://doi.org/10.1038/ngeo2343>
- Uenishi, K., & Rice, J. R. (2003). Universal nucleation length for slip-weakening rupture instability under nonuniform fault loading. *Journal of Geophysical Research*, 108(B1), 2042. <https://doi.org/10.1029/2001jb001681>
- Urata, Y., Yamashita, F., Fukuyama, E., Noda, H., & Mizoguchi, K. (2018). Apparent dependence of rate-and state-dependent friction parameters on loading velocity and cumulative displacement inferred from large-scale biaxial friction experiments. In *Earthquakes and multi-hazards around the Pacific Rim* (Vol. I, pp. 23–43). Springer.
- Viesca, R. C. (2016). Stable and unstable development of an interfacial sliding instability. *Physical Review E*, 93(6), 060202. <https://doi.org/10.1103/physreve.93.060202>
- Voss, N., Dixon, T. H., Liu, Z., Malservisi, R., Protti, M., & Schwartz, S. (2018). Do slow slip events trigger large and great megathrust earthquakes? *Science Advances*, 4(10), eaat8472. <https://doi.org/10.1126/sciadv.aat8472>
- Yamada, T., Mori, J. J., Ide, S., Abercrombie, R. E., Kawakata, H., Nakatani, M., et al. (2007). Stress drops and radiated seismic energies of microearthquakes in a south african gold mine. *Journal of Geophysical Research*, 112(B3), B03305. <https://doi.org/10.1029/2006jb004553>
- Yamashita, F., Fukuyama, E., Xu, S., Kawakata, H., Mizoguchi, K., & Takizawa, S. (2021). Two end-member earthquake preparations illuminated by foreshock activity on a meter-scale laboratory fault. *Nature Communications*, 12(1), 1–11. <https://doi.org/10.1038/s41467-021-24625-4>
- Yao, D., Huang, Y., Peng, Z., & Castro, R. R. (2020). Detailed investigation of the foreshock sequence of the 2010  $M_w$  7.2 el mayor-cucapah earthquake. *Journal of Geophysical Research: Solid Earth*, 125(6), e2019JB019076. <https://doi.org/10.1029/2019jb019076>
- Yoshimitsu, N., Kawakata, H., & Takahashi, N. (2014). Magnitude-7 level earthquakes: A new lower limit of self-similarity in seismic scaling relationships. *Geophysical Research Letters*, 41(13), 4495–4502. <https://doi.org/10.1002/2014gl060306>